

CLUSTER MORPHOLOGIES AND MODEL-INDEPENDENT Y_{SZ} ESTIMATES FROM BOLOCAM
SUNYAEV-ZEL'DOVICH IMAGESJ. SAYERS^{1,3}, S. R. GOLWALA¹, S. AMEGLIO², AND E. PIERPAOLI²*Draft version October 28, 2018*

ABSTRACT

We present initial results from our ongoing program to image the Sunyaev-Zel'dovich (SZ) effect in galaxy clusters at 143 GHz using Bolocam; five clusters and one blank field are described in this manuscript. The images have a resolution of 58 arcsec and a radius of $\simeq 6 - 7$ arcmin, which is approximately $r_{500} - 2r_{500}$ for these clusters. We effectively high-pass filter our data in order to subtract noise sourced by atmospheric fluctuations, but we are able to obtain unbiased images of the clusters by deconvolving the effects of this filter. The beam-smoothed RMS is $\simeq 10 \mu\text{K}_{CMB}$ in these images; with this sensitivity we are able to detect SZ signal to beyond r_{500} in binned radial profiles. We have fit our images to beta and Nagai models, fixing spherical symmetry or allowing for ellipticity in the plane of the sky, and we find that the best-fit parameter values are in general consistent with those obtained from other X-ray and SZ data. Our data show no clear preference for the Nagai model or the beta model due to the limited spatial dynamic range of our images. However, our data show a definitive preference for elliptical models over spherical models, quantified by an F -ratio of $\simeq 20$ for the two models. The weighted mean ellipticity of the five clusters is $\epsilon = 0.27 \pm 0.03$, consistent with results from X-ray data. Additionally, we obtain model-independent estimates of Y_{500} , the integrated SZ y -parameter over the cluster face to a radius of r_{500} , with systematics-dominated uncertainties of $\simeq 10\%$. Our Y_{500} values, which are free from the biases associated with model-derived Y_{500} values, scale with cluster mass in a way that is consistent with both self-similar predictions and expectations of a $\simeq 10\%$ intrinsic scatter.

Subject headings: cosmology: observation — galaxies: clusters: individual (Abell 697, Abell 1835, MS 0015.9+1609, MS 0451.6-0305, MS 1054.4-0321) — methods: data analysis

1. INTRODUCTION

Galaxy clusters are the largest collapsed objects in the universe, making them excellent tools for studying cosmology and the astrophysics of gravitational collapse. They are rare excursions in the matter density field and the formation history of clusters is closely tied to the composition and evolution of the universe. As a consequence, clusters have been used extensively to constrain cosmology. For example, they provided the first evidence that the matter density, Ω_m , was insufficient to close the universe (Bahcall et al. 1997). Additionally, clusters provided the most reliable information about the amplitude of scalar perturbations, σ_8 , prior to the release of WMAP results (Viana and Liddle 1999; Pierpaoli et al. 2001, 2003; Borgani et al. 2001; Allen et al. 2003a; Spergel et al. 2003).

Moreover, the cluster-derived measurements of σ_8 can be combined with measurements of the normalization of the CMB power spectrum to constrain the total neutrino mass via the growth of density perturbations (Pierpaoli 2004; Allen et al. 2003b; Vikhlinin et al. 2009). In addition, galaxy clusters have been forming during the same epoch that dark energy has evolved to dominate the energy density the universe. As a result, the number of galaxy clusters as a function of redshift is sensitive to the dark energy density, Ω_λ , and its equation of state, w (Haiman et al. 2001; Holder et al. 2000, 2001). Recently, large surveys of galaxy clusters have been com-

pleted, or have released initial results, that constrain the total neutrino mass and/or the properties of dark energy (Allen et al. 2008; Mantz et al. 2010a; Vikhlinin et al. 2009; Vanderlinde et al. 2010). Additionally, clusters are being used to test gravity on large scales via studies of their internal structure and distribution in space (Schmidt et al. 2009; Diaferio and Ostorero 2009; Martino et al. 2009; Wu et al. 2010; Moffat and Toth 2010; Rapetti et al. 2010).

Galaxy clusters also provide excellent laboratories for studying the astrophysics of structure formation. In general, galaxy clusters are well-behaved objects, and their properties can be predicted to fairly good precision using simple gravitational collapse models and self-similar scaling relations (Kaiser 1986). However, non-gravitational effects, such as radiative cooling, star formation, turbulence, magnetic field support, and cosmic ray pressure produce deviations from the simple gravitational models, and the data clearly favor models that include non-gravitational processes (Kravtsov et al. 2006; Nagai et al. 2007).

A wide range of observational techniques are used to study galaxy clusters. Optical/infrared and radio measurements can be used to study the individual galaxies within the cluster (*e.g.*, Pipino et al. (2010); Lin et al. (2009); Gralla et al. (2010)); parameters such as velocity dispersion and richness can then be used to understand the global properties of the cluster (*e.g.*, Menanteau et al. (2010a); Rines and Diaferio (2010); Serra et al. (2010); Szabo et al. (2010); Hao et al. (2010)). Additionally, X-ray observations are sensitive to the bremsstrahlung

¹ California Institute of Technology, Pasadena, CA 91125² University of Southern California, Los Angeles, CA 90089³ jack@caltech.edu

emission from the hot gas in the intra-cluster medium (ICM), which contains $\simeq 90\%$ of the baryonic mass of the cluster (*e.g.*, Vikhlinin et al. (2006); Gonzalez et al. (2007); Vikhlinin et al. (2009); Arnaud et al. (2009); Zhang et al. (2010)). Galaxy clusters are also efficient gravitational lenses, and detailed observations of the background galaxies can be used to determine the matter distribution within the cluster, $\simeq 90\%$ of which is in the form of dark matter (Clowe et al. 2006; Allen et al. 2008).

The ICM can also be studied using the Sunyaev-Zel'dovich (SZ) effect (Sunyaev and Zel'dovich 1972), where the background CMB photons inverse Compton scatter off of the electrons in the ICM. Studies of galaxy clusters using the SZ effect are quickly maturing. The South Pole Telescope (SPT) and the Atacama Cosmology Telescope (ACT) are conducting large untargeted surveys and have already published catalogues with dozens of clusters (Vanderlinde et al. 2010; Menanteau et al. 2010b); they expect to detect hundreds of clusters when the surveys are complete. Due to the redshift independence of the SZ surface brightness, the clusters discovered in these surveys are, on average, at significantly higher redshifts than those discovered with X-ray or optical surveys. Consequently, SZ-selected cluster catalogues are expected to play a leading role in further constraining cosmological parameters such as Ω_Λ and w (*e.g.*, Carlstrom et al. (2002)).

These large-scale SZ surveys are operating based on the prediction that the total integrated SZ signal over the cluster, Y , which is proportional to the total thermal energy of the ICM, scales in a robust way with total cluster mass (*e.g.*, Kravtsov et al. (2006)). In practice, the integral does not generally extend to the edge of the cluster, which is effectively at $\gtrsim 5r_{500}$, and can be performed in one of two ways: over a spherical volume using a deprojected SZ profile or over a cylindrical volume using a projected SZ profile. Most groups have calculated the integrated SZ signal by performing the cylindrical integration over the cluster face within a well defined aperture (generally r_{2500} or r_{500}) (Morandi et al. 2007; Bonamente et al. 2008; Mroczkowski et al. 2009; Marrone et al. 2009; Plagge et al. 2010; Huang et al. 2010; Culverhouse et al. 2010; Andersson et al. 2010), although a couple groups have also performed the spherical integral (Mroczkowski et al. 2009; Andersson et al. 2010). With the exception of Plagge et al. (2010, hereafter P10), these groups have exclusively used parametric profiles to describe the SZ signal in order to determine Y . The initial scaling results from these Y measurements are roughly consistent with the expectation that it is a low-scatter ($\simeq 10\%$) proxy for the total cluster mass.

Additionally, several groups have made detailed SZ observations of previously known galaxy clusters, and these data have been used to constrain the properties of the ICM beyond r_{500} (Halverson et al. 2009; Nord et al. 2009; Basu et al. 2010; Mroczkowski et al. 2009; Plagge et al. 2010). For example, the SPT has measured radial profiles in 15 clusters to a significant fraction of the virial radius, and they find best-fit model parameters that are consistent with previous studies using X-ray data P10. APEX-SZ has published detailed studies of three clusters, using a joint SZ/X-ray analysis to constrain mass-weighted temperature profiles be-

yond r_{500} in two of these clusters (Halverson et al. 2009; Nord et al. 2009; Basu et al. 2010). Note that, in addition to providing complementary information about the ICM in these previously studied clusters, these SZ data will help constrain and improve systematic uncertainties in blind SZ surveys (*e.g.*, constraining the typical SZ profiles and resulting detection biases due to the cooling properties of the central gas (Pipino and Pierpaoli 2001)).

High resolution ($\simeq 10$ arcsec) SZ measurements are also now being made using MUSTANG (Mason et al. 2010; Korngut et al. 2010) and SZA/CARMA (Carlstrom et al. 2002). These observations will provide insights on the internal structure of clusters that will be complementary to the information obtained via X-ray observations. Among other applications, these data can be used, in combination with optical observations, to infer the merging history and evolution of the cluster (Croston et al. 2008).

In this work, we present Bolocam SZ observations of five massive galaxy clusters. We are able to measure SZ signal in our two-dimensional images to $\simeq r_{500}$ and to well beyond r_{500} in azimuthally averaged radial profiles. Using these data, we are able to constrain the broad morphologies of these clusters and compute observables such as Y_{SZ} in a model-independent way. A companion paper to this manuscript, Ameglio et al. (2010), presents joint X-ray/SZ deprojections of density and temperature profiles for these same five clusters using Bolocam and *Chandra* data (Ameglio et al. 2007).

2. CLUSTER OBSERVATIONS WITH BOLOCAM

Bolocam is a mm-wave imaging camera that operates from the Caltech Submillimeter Observatory (CSO) with 144 bolometric detectors covering a circular 8 arcmin field of view (FOV) (Glenn et al. 1998; Haig et al. 2004). For the observations described in this manuscript, Bolocam was configured to observe at 143 GHz. To image the clusters, we scanned the telescope in a Lissajous pattern (Kovacs et al. 2006), where the telescope is driven in two orthogonal directions using sine waves with incommensurate periods. We used an amplitude of 4 arcmin for the sinusoids, which were oriented along the RA and dec directions with periods of 6.28 and 8.89 sec. These parameters were chosen to keep the FOV on the cluster center 100% of the time while scanning as fast as possible at the CSO ($\simeq 4$ arcmin/sec) to modulate the cluster signal above the low-frequency atmospheric noise. An example of the resulting integration time per pixel is given in Figure 1. The data were collected via 10-minute-long observations, with the periods of the two orthogonal sinusoids exchanged between observations. Typically, we complete $\simeq 100$ observations per cluster, which corresponds to approximately 50 ksec and yields a beam-smoothed RMS of $\simeq 10 \mu\text{K}_{CMB}$ (see Table 1).

In this paper, we present the results from five clusters and one blank field, which are described below. Due to the size of our resulting maps ($r \simeq 6 - 7$ arcmin), we have chosen to focus primarily on high-redshift clusters, which have virial radii within the extent of our maps. All of the clusters presented in this manuscript are beyond $z = 0.25$, and three of the five are beyond $z = 0.50$. For reference, r_{500} lies within the extent of our map for a typical $10^{15} M_\odot$ cluster at $z = 0.25$, and at $z = 0.50$, the

TABLE 1
CLUSTER PROPERTIES

target	RA	dec	redshift	Bolocam time (ksec)	RMS (μK_{CMB})	r_{500} (Mpc)	$M_{gas,500}$ (M_{\odot})
Abell 697	08:42:58	+36:21:56	0.28	52	8.9	1.65 ± 0.09	$19.6 \pm 2.7 \times 10^{13}$
Abell 1835	14:01:02	+02:52:42	0.25	50	8.7	1.49 ± 0.06	$14.1 \pm 1.2 \times 10^{13}$
MS 0015.9+1609	00:18:34	+16:26:13	0.54	38	10.2	1.28 ± 0.08	$17.5 \pm 1.9 \times 10^{13}$
MS 0451.6-0305	04:54:11	-03:00:53	0.55	53	7.7	1.45 ± 0.12	$15.6 \pm 2.2 \times 10^{13}$
MS 1054.4-0321	10:56:59	-03:37:34	0.83	66	6.7	1.07 ± 0.13	$11.5 \pm 2.4 \times 10^{13}$
SDS1	02:18:00	-05:00:00	-	37	9.1	-	-

NOTE. — A list of the clusters presented in this manuscript. From left to right the columns give the RA and dec of the cluster in J2000 coordinates, the redshift of the cluster, the amount of Bolocam integration time, the median RMS per beam-smoothed pixel in the Bolocam map, the radius of the cluster, and the mass of the cluster. The values for r_{500} and $M_{gas,500}$ were taken from Mantz et al. (2010b) (Abell 697 and Abell 1835) and Ettori et al. (2009) (MS 0015.9+1609, MS 0451.6-0305, and MS 1054.4-0321)

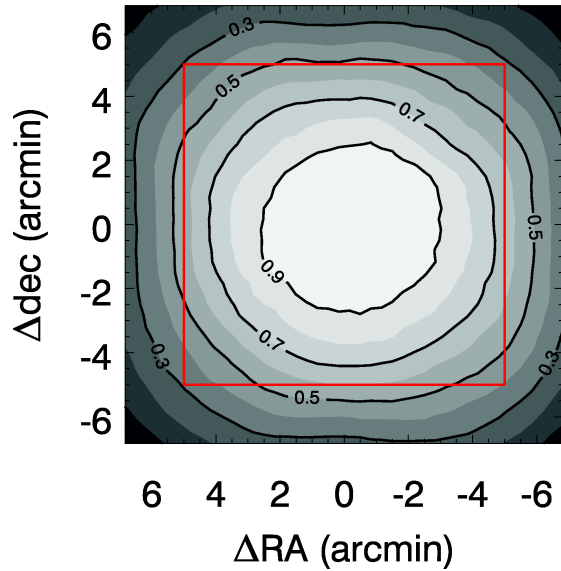


FIG. 1.— Integration time per pixel, relative to the maximum integration time, for MS 0451.6-0305. Our model fits include all of the data within a circular region with a minimum integration time of 25% of the peak integration time, which corresponds to 6 – 7 arcmin in radius. The red box, with 10 arcmin sides, denotes the region used for deconvolution of the processing transfer function. The minimum relative integration time within this region is also $> 25\%$.

virial radius lies within our map. Note that, throughout this work, we assume a Λ CDM cosmology with $\Omega_m = 0.3$, $\Omega_\Lambda = 0.7$, and $H_0 = 70$ km/s/Mpc.

Abell 697: Abell 697 is a cluster undergoing a complex merger event along the line of sight (Girardi et al. 2006).

Abell 1835: Abell 1835 is a relaxed cluster with a strong cooling flow (Peterson et al. 2001; Schmidt et al. 2001).

MS 0015.9+1609: MS 0015.9+1609 is a triaxial cluster that is elongated along the line of sight and has an anomalously high gas mass fraction of 27% (Piffaretti et al. 2003).

MS 0451.6-0305: MS 0451.6-0305 is a cluster that is not quite in gravitational equilibrium, with a slightly elongated X-ray profile (Donahue et al. 2003).

MS 1054.4-0321: MS 1054.4-0321 is a cluster undergoing a merger, as evidenced by the presence of two distinct sub-clumps in the X-ray image (Jeltema et al. 2001; Jee et al. 2005).

SDS1: Our SDS1 map is centered in the middle of the Subaru/XMM Deep Survey (SXDS) field. The deep *XMM-Newton* survey of this field reveals only 3 clusters within our map, all near the edge, and the largest of which has a virial mass of $M_{200} = 0.8 \times 10^{13} M_{\odot}$ (Finoguenov et al. 2010). Therefore, SDS1 is approximately free of signal from the SZ effect.

3. DATA REDUCTION

In general, our data reduction followed the procedure described in Sayers et al. (2009, hereafter S09), with some minor modifications. We briefly describe the techniques below, along with the changes relative to S09.

3.1. Calibration

Bright quasars located near the clusters were observed for 10 minutes once every $\simeq 90$ minutes in order to determine the offset of our focal plane relative to the telescope pointing coordinates. These observations were used to construct a model of the pointing offset as a function of local coordinates (az,el), with a single model for each cluster. The uncertainty in the pointing models is $\lesssim 5$ arcsec. This pointing uncertainty is quasi-negligible for Bolocam's 58 arcsec FWHM beams, especially for extended objects such as clusters. We made two 20-minute-long observations each night of Uranus, Neptune, or a source in Sandell (1994) for flux calibration. Using the quiescent detector resistance as a proxy for detector responsivity and atmospheric transmission, we then fit a single flux-calibration curve to the entire data set. We estimate the uncertainty in our flux calibration to be 4.3%, with the following breakdown: 1.7% from the Rudy temperature model of Mars scaled to measured WMAP values (Halverson et al. 2009; Wright 1976; Griffin et al. 1986; Rudy et al. 1987; Muhleman and Berge 1991; Hill et al. 2009), 1.5% in the Uranus/Neptune model referenced to Mars (Griffin and Orton 1993), 1.4% due to variations in atmospheric opacity (S09), 3.1% due to uncertainties in the solid angle of our point-spread function (PSF) (S09), and 1.5% due to measurement uncertainties (S09).

3.2. Atmospheric noise subtraction

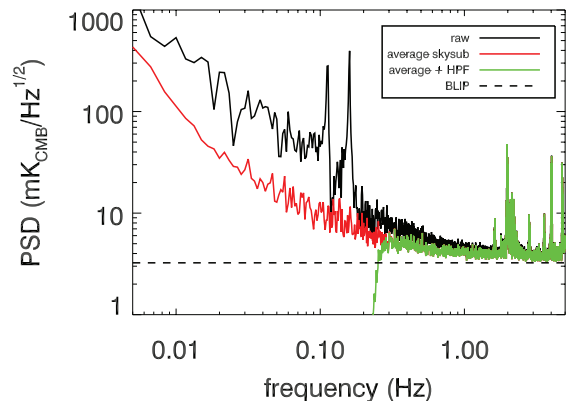


FIG. 2.— Timestream noise PSD for a typical Bolocam detector. The black curve shows the raw PSD recorded by the detector; spectral lines at the fundamental scan frequencies are clearly seen above the broadband atmospheric noise. The red curve shows the noise PSD after subtracting the atmospheric noise using the average signal over the FOV. This timestream is then high-pass filtered at 250 mHz to produce the green PSD. Note that there is very little cluster signal above $\simeq 2$ Hz, where there are some spectral lines due to the readout electronics. The dashed horizontal line provides an estimate of the photon, or BLIP, noise.

The raw Bolocam timestreams are dominated by noise sourced by fluctuations in the water vapor in the atmosphere, which have a power spectrum that rises sharply at low frequencies. In order to optimally subtract the atmospheric noise, we have used a slightly modified version of the average subtraction algorithm described in Sayers et al. (2010, hereafter S10). We have modified the S10 algorithm because these cluster data contain additional atmospheric noise caused by the Lissajous scan pattern. Since we are scanning the telescope parallel to RA and dec, the airmass we are looking through is constantly changing. As a result, our data contain a large amount of atmospheric signal in narrow bands centered on the two fundamental scan frequencies.

Following the algorithm in S10, we first create a template of the atmosphere by averaging the signal from all of our detectors at each time sample (*i.e.*, the average signal over the FOV). In S10, this template is subtracted from each detector’s timestream after weighting it by the relative gain of that detector, which is determined from the correlation coefficient between the timestream and the template. We use a single correlation coefficient for each detector for each 10-minute-long observation. However, a significant fraction of the atmospheric noise at the fundamental scan frequencies remains in the data after application of the S10 algorithm, indicating that we have slightly misestimated the correlation coefficients. Therefore, we modified the S10 algorithm to compute the correlation coefficients for the template based only on the data within a narrow band centered on the two fundamental scan frequencies. The atmospheric noise power in these narrow frequency bands is roughly an order of magnitude above the broadband atmospheric noise at nearby frequencies; consequently, the data in these narrow bands provide a high signal-to-noise estimate of each detector’s response to atmospheric signal. The narrow-band atmospheric noise features are completely removed using this modified S10 algorithm, and the amount of residual broadband atmospheric noise is slightly reduced compared to the results from the original S10 algorithm.

After applying this average subtraction algorithm to

the timestream data, we then high-pass filter the data according to

$$\mathcal{F} = 1 - \frac{1}{1 + (10f/f_0 - 1)^\kappa}$$

with $f_0 = 250$ mHz and $\kappa = 8$. The value of f_0 was chosen to maximize the spatially-extended S/N for the typical cluster in our sample based on tests with f_0 varying from 0 to 400 mHz, and the value of κ was chosen to produce a sharp cutoff with minimal ringing. Figure 2 shows a typical pre and post-subtraction timestream noise PSD.

3.3. Transfer function of the atmospheric noise filtering

In addition to subtracting atmospheric noise, the FOV-average subtraction and timestream high-pass filter also remove some cluster signal. Since we use the data timestreams to both determine the atmospheric fluctuation template and the correlation coefficient of each detector’s data timestream with the template, the FOV-average subtraction acts on the data in a non-linear way. Consequently, its impact on the data depends on the cluster signal. As described below, we quantify the effects of the FOV-average subtraction and the timestream high-pass filter via simulation by processing a known cluster image through our data-reduction pipeline. These simulations are computation-time intensive, and we find, in practice (see Section 6.1), that the filtering is only mildly dependent on the cluster signal. Thus, in the end, we determine the effects of the filtering for a particular cluster’s data set using the cluster model that best fits those data. We use the term transfer function to describe the effect of the filtering, although this terminology is not rigorously correct because the filtering depends in the cluster signal.

To compute the transfer function, we first insert a simulated, beam-smoothed cluster profile into our data timestreams by reverse mapping it using our pointing information. These data are then processed in an identical way to the original data, and an output image, or map, is produced. When processing the data-plus-simulated-cluster timestreams we use the FOV-average subtraction correlation coefficients that were determined for the original data. This ensures that the simulated cluster is processed in an identical way to the real cluster in our data. In the limit that the best-fit cluster model is an accurate description of the data, this process is rigorously correct. The original data map is then subtracted from this data-plus-simulated-cluster map to produce a noise-free image of the processed cluster. In Figure 3, we show an example cluster image, along with the noise-free processed image of the same cluster. The Fourier transform of this processed cluster image is divided by the Fourier transform of the input cluster to determine how the cluster is filtered as a function of 2-dimensional Fourier mode (*i.e.*, what we term the transfer function, see Figure 4).

At small angular scales, there is very little signal in the beam-smoothed input cluster, and numerical noise prevents us from accurately characterizing the transfer function at these scales. The transfer function is expected to be unity at small angular scales, and is asymptoting to this value at the larger scales where we can accurately characterize it. Therefore, we set the transfer function to a value of 1 for $u > 0.75$ arcmin $^{-1}$. Deconvolving the

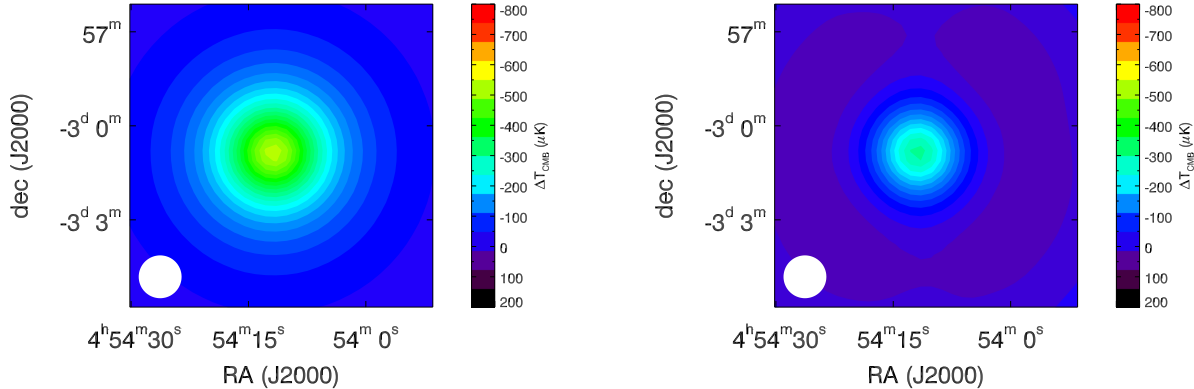


FIG. 3.— Images of the best-fit spherical Nagai model for MS 0451.6-0305. The left image is the model and the right image is the model after being processed through our data reduction pipeline, which high-pass filters the image in a complex way. This filtering significantly reduces the peak decrement of the cluster and creates a ring of positive flux at $r \gtrsim 2$ arcmin. Note that the processed image is not quite azimuthally symmetric.

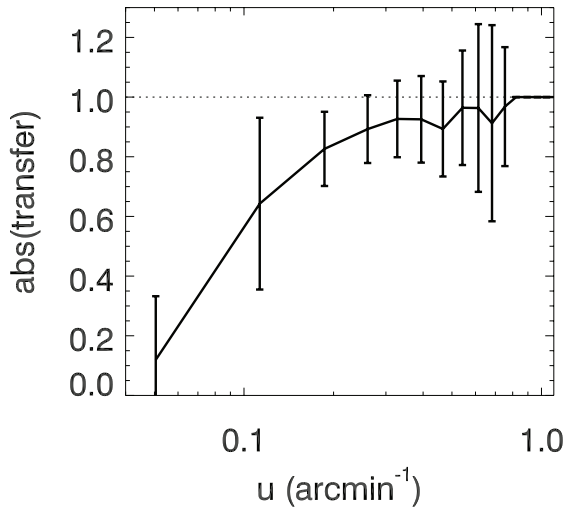


FIG. 4.— The magnitude of the transfer function for MS 0451.6-0305 as a function of Fourier wavenumber $u = 1/\lambda$. At large scales, or small u , the measurement error is negligible and the error bars provide an indication of the azimuthal variation. At $u > 0.75$ arcmin $^{-1}$, the measurement error becomes non-negligible and we set the transfer function equal to 1. Note that this azimuthally averaged transfer function is for display purposes only; we have used the full two-dimensional transfer function throughout our analysis.

processed cluster image using the transfer function (see Section 5), which has been approximated as 1 at small angular scales, produces an image that is slightly biased compared to the input cluster. The residuals between these two images are approximately white, with an RMS of $\lesssim 0.1 \mu\text{K}_{\text{CMB}}$. This transfer-function-induced bias is negligible compared to our noise, which has an RMS of $\simeq 10 \mu\text{K}_{\text{CMB}}$.

As noted above, the transfer function (weakly) depends on the profile of the cluster; larger clusters are more heavily filtered than smaller clusters. Therefore, we determine a unique transfer function for each cluster using the best-fit elliptical Nagai model for that cluster (Nagai et al. 2007, hereafter N07). The details of this fit are given in Section 4. Since the transfer function depends on the best-fit model, and vice versa, we determine the best-fit model and transfer function in an iterative way. Starting with a generic cluster profile, we

first determine a transfer function, and then fit an elliptical Nagai model using this transfer function (*i.e.*, the Nagai model parameters are varied while the transfer function is held fixed). This process is repeated, using the best-fit model from the previous iteration to calculate the transfer function, until the best-fit model parameters stabilize. This process converges fairly quickly, usually after a single iteration for the clusters in our sample. The model dependence of the resulting transfer function is quantified in Section 6.1.

3.4. Noise estimation

In order to accurately characterize the sensitivity of our images, we compute our map-space noise directly from the data via 1000 jackknife realizations of our cluster images. In each realization, random subsets of half of the $\simeq 100$ observations are multiplied by -1 prior to adding them into the map. Each jackknife preserves the noise properties of the map while removing all of the astronomical signal, along with any possible fixed-pattern or scan-synchronous noise due to the telescope scanning motion⁴. Since these jackknife realizations remove all astronomical signal, we estimate the amount of astronomical noise in our images separately, as described below. After normalizing the noise estimate of each map pixel in each jackknife by the square root of the integration time in that pixel, we construct a sensitivity histogram, in $\mu\text{K}_{\text{CMB}}\text{-s}^{1/2}$, from the ensemble of map pixels in all 1000 jackknives. The width of this histogram provides an accurate estimate of our map-space sensitivity (see Figure 5). We then assume that the noise covariance matrix is diagonal⁵ and divide by the square root of the integration time in each map pixel to determine the noise RMS in that pixel. This method is analogous to the one used in S09, where it is described in more detail.

There is a non-negligible amount of noise in our

⁴ We show that there is no measurable fixed-pattern or scan-synchronous noise in our data later in this section and in Section 6.2.

⁵ This approximation is justified for our processed data maps in Section 6.2. Note that the approximation fails for our deconvolved images (see Section 5), which contain a non-negligible amount of correlated noise. We describe how this correlated noise is accounted for in our results in Section 5.

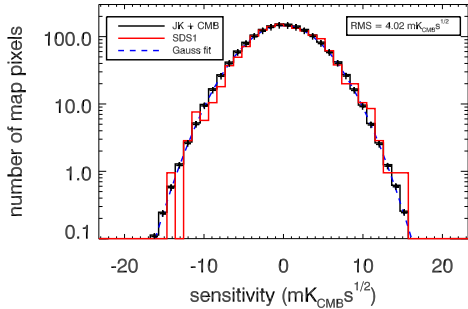


FIG. 5.— Histogram of the per-pixel sensitivity for our maps of the blank-field SDS1. The black line shows the average histogram for each of the 1000 jackknife realizations of the data, with noise from the CMB and unresolved point sources added as described in Section 3.4. The sensitivities derived from the noise realizations are well described by a Gaussian fit, with the fit quality quantified by a PTE of 0.44. Overlaid in red is the histogram for our map of SDS1, which is also well described by the Gaussian fit to the noise realizations (PTE = 0.63), indicating that our noise model adequately describes the data. The dashed blue line shows the best-fit Gaussian to the noise realizations and has an RMS of $4.02 \mu\text{K}_{\text{CMB}}\text{-s}^{1/2}$.

maps from two main types of astronomical sources: anisotropies in the CMB and unresolved point sources. The South Pole Telescope (SPT) has recently published power spectra for both of these sources at 150 GHz over the range of angular scales probed by our maps, so we use their measurements to estimate the astronomical noise in our maps (Lueker et al. 2010; Hall et al. 2010). Note that these measurements inherently include all astrophysical effects, such as lensing and clustering of point sources. Using the SPT power spectra, we generate simulated maps of our cluster fields assuming Gaussian fluctuations. Note that this is a poor assumption for both the SZ-sourced CMB fluctuations and the signal sourced by background galaxies that are lensed by the cluster. However, since the noise power from both of these sources is quasi-negligible compared to the total noise in our images, any failure of our Gaussian assumption will have a minimal impact on our results. The good match of the SDS1 data to our noise model validates our Gaussian assumption (see Figure 5). These simulated images of the CMB plus point sources are then reverse mapped into our timestream data and processed to estimate how they will appear in our cluster maps. We then add these processed astronomical realizations to our jackknife realizations to provide a complete estimate of the noise in our images. Sensitivity estimates from our signal-free map of SDS1 agree well with the sensitivity estimates from our noise maps, indicating that there are no additional noise sources that have not been included in our estimate (see Figure 5). The properties of this noise are described in more detail in Section 6.2. In general, the noise from astronomical sources is quasi-negligible compared to the other noise in our images. However, the large-scale correlations from CMB fluctuations are non-negligible in our deconvolved images (see Table 5).

Note that we have chosen to model the signal from point sources as an additional noise term in our maps rather than attempting to subtract any individual point sources. Part of the motivation for this approach is the fact that we do not detect any point sources in our cluster

or blank-field images. For reference, P10 mapped 15 clusters to a similar depth using the SPT and only detected two point sources; the combined area of the SPT images is approximately 20 times the combined area of our 6 images. Although there are several known SMGs and AGNs in our images (Zemcov et al. 2007; Ivison et al. 2000; Cooray et al. 1998), even the brightest sources will have a flux of $\simeq 10 \mu\text{K}_{\text{CMB}}$ in our observing band, rendering them undetectable given our noise RMS of $\simeq 10 \mu\text{K}_{\text{CMB}}$. Additionally, it is not possible to reliably estimate the flux of these sources in our observing band since most have only been detected at one or two wavelengths, generally separated from our observing band by more than a factor of 2 in wavelength.

4. CLUSTER MODEL FITTING

4.1. The SZ effect

As mentioned above, the SZ effect involves CMB photons inverse Compton scattering off of hot electrons in the ICM. Since the electrons are many orders of magnitude hotter than the CMB photons, there is, on average, a net increase in the energy of the photons. The classical distortion relative to the blackbody spectrum of the CMB is given by

$$f(x) = x \frac{e^x + 1}{e^x - 1} - 4,$$

where $x = h\nu/k_B T_{\text{CMB}}$. The magnitude of the distortion is proportional to the product of the density and temperature of the electrons in the ICM projected along the line of sight. The frequency-dependent temperature change of the CMB is given by

$$T_{\text{SZ}} = f(x)yT_{\text{CMB}},$$

where

$$y = \int n_e \sigma_T \frac{k_B T_e}{m_e c^2},$$

and n_e and T_e are the density and temperature of the ICM electrons. Relativistic corrections can be included by multiplying $f(x)$ by $(1 + \delta(x, T_e))$ (Itoh et al. 1998). Note that the X-ray brightness of the ICM is proportional to $n_e^2 T_e^{1/2}$; the differing density and temperature dependence of the SZ and X-ray signals makes them highly complementary probes of the ICM (*e.g.*, Bonamente et al. (2006), hereafter B06).

4.2. Models

We have fit our data to two types of models: an isothermal beta model (Cavaliere and Fusco-Femiano 1976, 1978) and the pressure profile proposed by N07, hereafter the Nagai profile. The isothermal beta model has been used extensively to describe X-ray and SZ measurements of the ICM, and our beta model fit parameters can be directly compared to these previous results. However, the beta model provides a poor description of deep X-ray data, which generally have a cuspiest core and steeper outer profile (*e.g.*, Vikhlinin et al. (2006), N07, and Arnaud et al. (2009)). In contrast, the Nagai pressure profile, which is a generalization of the NFW dark matter profile, is able to describe deep X-ray observations over a wide range of scales (N07, Arnaud et al. (2009)). Therefore, we have also fit our data to the Nagai model.

In practice, the beta and Nagai models are highly degenerate over the range of angular scales to which our data are sensitive (1 – 12 arcmin).

Specifically, the isothermal beta model is described by

$$p = \frac{p_0}{(1 + r^2/r_c^2)^{3\beta/2}},$$

where p is the pressure profile, p_0 is the pressure normalization, r_c is the core radius, and β is the power law slope. The beta model can be analytically integrated along the line of sight to give the observed SZ signal, with

$$T_{SZ} = \frac{f(x)y_0 T_{CMB}}{(1 + r^2/r_c^2)^{(3\beta-1)/2}} + \delta T,$$

where T_{SZ} is the SZ signal in our map (in μK_{CMB}) and y_0 is the central Comptonization. We fix the value of β at 0.86 for all of our fits; this is the best-fit value found in P10 for SZ data⁶. Since our data timestreams are high-pass filtered, we are not sensitive to the DC signal level in our images. Note that because the timestream data, rather than the map, are high-pass filtered, the DC signal level of the map is in general not equal to 0. However, the DC signal of the map is not physically meaningful due to the filtering and must therefore be included as a free parameter, δT , in the model fits. We have also generalized the beta model to be elliptical in the plane of the sky with

$$T_{SZ} = \frac{f(x)y_0 T_{CMB}}{(1 + \frac{r_1^2}{r_c^2} + \frac{r_2^2}{(1-\epsilon)^2 r_c^2})^{(3\beta-1)/2}} + \delta T,$$

where r_1 is oriented along the major axis, described by a position angle of θ (in degrees east of north), r_2 is orthogonal to the major axis, and ϵ is the ellipticity.

The Nagai model is described by

$$p = \frac{p_0}{(r/r_s)^C [1 + (r/r_s)^C]^{(\mathcal{B}-C)/\mathcal{A}}}, \quad (1)$$

where p is the pressure, p_0 is the pressure normalization, r_s is the scale radius ($r_s = r_{500}/c$, with $c \simeq 1.2$ (Arnaud et al. 2009)), and \mathcal{A} , \mathcal{B} , and \mathcal{C} are the power law slopes at intermediate, large, and small radii compared to r_s . We have fixed the values of \mathcal{A} , \mathcal{B} , and \mathcal{C} to the best-fit values found in Arnaud et al. (2009) (1.05, 5.49, 0.31). The Nagai model is not analytically integrable, so we numerically integrate p along the line of sight to determine T_{SZ} . We have also generalized the Nagai model to be elliptical in the plane of the sky, using the same notation as our elliptical generalization of the beta model. Note that, in all of our fits, we have corrected for relativistic effects via the approximations given in Itoh et al. (1998) using gas temperature estimates from X-ray observations of these clusters (Cavagnolo et al. 2008; Jeltama et al. 2001). The relativistic corrections are $\simeq 5\%$ for the typical temperatures in these massive clusters ($\simeq 10$ keV).

We find that both the beta model and the Nagai model adequately describe our data, with the exception of Abell

697, and neither model is preferred with any significance. However, the elliptical models ($\chi^2/\text{DOF} = 5605/5413$) provide a much better fit to the full ensemble of our cluster data compared to the spherical models ($\chi^2/\text{DOF} = 5813/5423$, see Tables 2 and 3). The F -ratio for these two fits is 20.1 for $\nu_1 = 10$ and $\nu_2 = 5413$ degrees of freedom (Bevington and Robinson 1992), corresponding to a probability of $< 10^{-36}$ that we would obtain data with equal or greater preference for elliptical models if the clusters were spherical. If we neglect Abell 697, which is not well described by either model, then the F -ratio is 12.2 with a corresponding probability of $< 10^{-16}$. The weighted mean ellipticity of the five clusters is $\epsilon = 0.27 \pm 0.03$, consistent with results from X-ray data (*e.g.*, Maughan et al. (2008); De Filippis et al. (2005)). Our inability to distinguish between the Nagai and beta models is likely due to the limited spatial dynamic range of our images ($\simeq 1 - 12$ arcmin). For the clusters in our sample, we are insensitive to the core, $r \lesssim 0.15 r_{500} \simeq 0.5$ arcmin, and the outskirts of the cluster $r \gtrsim 2 r_{500} \simeq 10$ arcmin, which means we are only sensitive to a single power law exponent in the Nagai model, \mathcal{A} . For this reason, the Nagai model is highly degenerate with the beta model for the angular scales probed by our data.

4.3. Fitting procedure

Our cluster images are filtered by both the atmospheric noise subtraction and the Bolocam point-spread function. Therefore, prior to fitting a model to our data, we need to filter the cluster model in an identical way. First, we generate a 2-dimensional image using the cluster model, computed directly from the isothermal beta model and via a line-of-sight integration of the Nagai pressure model. Next, the model image is convolved with the Bolocam point-spread function and the measured transfer function. In practice, the transfer function convolution is performed via multiplication in Fourier space. This filtered model is then compared to our data map, using all of the map pixels contained within a radius where the minimum coverage is greater than 25% of the peak coverage. This radius is typically between 6 and 7 arcmin. We use an iterative least-squares technique to determine the best-fit parameters for each model; we estimate the uncertainty on each parameter via the standard deviation of the best-fit parameter values estimated from noise realizations with model clusters added to them (see Section 6.2).

For each model, we fit both a scale radius (r_c for the beta model and r_s for the Nagai model) and a normalization (y_0 for the beta model and p_0 for the Nagai model). Additionally, as described above, we fit for the observationally unconstrained DC signal level of the map, δT . We also fit for a centroid offset relative to the X-ray pointing center. The offsets for the five clusters range from $\simeq 0 - 20 \pm 5$ arcsec, indicating there are no major differences in the X-ray and SZ centroids. Finally, when we allow the model to be elliptical in the image plane, we fit for the ellipticity ϵ and position angle θ . A complete list of the best-fit parameters for spherical and elliptical versions of both models is given in Tables 2 and 3.

4.4. Discussion and comparison to previous results

⁶ As P10 point out, this value for β is larger than those generally found from X-ray data, in agreement with simulations (Hallman et al. 2007). Additionally, it suggests that the ICM temperature is falling with increasing radius, in agreement with simulations and data (*e.g.*, N07).

TABLE 2
NAGAI MODEL FIT PARAMETERS

cluster	p_0 ($10^{-11} \frac{\text{erg}}{\text{cm}^3}$)	r_s (arcmin)	c_{500}	ϵ	θ (deg)	χ^2/DOF	PTE_{χ^2}	PTE_{sim}
elliptical Nagai model								
Abell 697	9.3 ± 1.3	6.9 ± 1.0	0.93 ± 0.14	0.37 ± 0.05	-24 ± 4	1289/1117	0.00	0.00
Abell 1835	8.1 ± 1.7	6.7 ± 1.5	0.94 ± 0.21	0.27 ± 0.07	-16 ± 10	966/945	0.31	0.22
MS 0015.9+1609	6.7 ± 1.4	5.5 ± 1.1	0.62 ± 0.13	0.24 ± 0.08	68 ± 12	1079/1117	0.79	0.73
MS 0451.6-0305	8.7 ± 1.6	4.7 ± 0.7	0.80 ± 0.14	0.26 ± 0.06	85 ± 7	1188/1117	0.07	0.08
MS 1054.4-0321	6.5 ± 1.9	3.6 ± 1.0	0.64 ± 0.19	0.09 ± 0.07	-1 ± 32	1084/1117	0.75	0.72
spherical Nagai model								
Abell 697	11.0 ± 1.8	4.6 ± 0.8	1.40 ± 0.22	-	-	1399/1119	0.00	0.00
Abell 1835	8.9 ± 2.1	5.1 ± 1.2	1.24 ± 0.27	-	-	1007/947	0.08	0.07
MS 0015.9+1609	6.0 ± 1.1	5.4 ± 1.1	0.63 ± 0.12	-	-	1100/1119	0.66	0.61
MS 0451.6-0305	10.6 ± 2.1	3.5 ± 0.5	1.08 ± 0.15	-	-	1220/1119	0.02	0.02
MS 1054.4-0321	6.0 ± 1.8	3.6 ± 1.0	0.64 ± 0.16	-	-	1087/1119	0.75	0.75

NOTE. — Table of the best-fit parameters and 1σ uncertainties for our Nagai model fits with the power-law exponents fixed to the best-fit values found in Arnaud et al. (2009) (1.05, 5.49, 0.31). From left to right the columns give the normalization of the Nagai profile, p_0 , the scale radius of the major axis, r_s , the concentration parameter, c_{500} , the ellipticity, ϵ , the position angle of the major axis in degrees east of north, θ , the χ^2 and DOF for the fit, and the goodness of fit quantified by the probability to exceed the given χ^2/DOF based on the standard χ^2 probability distribution function and also empirically by the fraction of our 1000 noise realizations that produce a larger χ^2 value when a model cluster is added to them (see Section 6.2). The values of c_{500} for the spherical fits can be compared to the nominal value of 1.17 that is given in Arnaud et al. (2009) based on spherical fits of X-ray data. See Section 6.2 for a description of how the parameter uncertainties are calculated. Note that we have included the 4.3% uncertainty in our flux calibration in the error estimates for p_0 .

TABLE 3
BETA MODEL FIT PARAMETERS

cluster	y_0 (10^{-4})	r_c (arcsec)	r_c/r_{500}	ϵ	θ (deg)	χ^2/DOF	PTE_{χ^2}	PTE_{sim}
elliptical beta model								
Abell 697	2.93 ± 0.26	98 ± 10	0.26 ± 0.03	0.38 ± 0.04	-10 ± 2	1288/1117	0.00	0.00
Abell 1835	2.49 ± 0.31	79 ± 11	0.21 ± 0.03	0.28 ± 0.07	-9 ± 10	970/945	0.28	0.20
MS 0015.9+1609	2.59 ± 0.27	85 ± 12	0.43 ± 0.07	0.24 ± 0.07	70 ± 12	1078/1117	0.79	0.73
MS 0451.6-0305	2.89 ± 0.22	68 ± 8	0.31 ± 0.04	0.26 ± 0.06	80 ± 8	1193/1117	0.06	0.06
MS 1054.4-0321	2.13 ± 0.22	58 ± 12	0.41 ± 0.10	0.09 ± 0.07	7 ± 33	1083/1117	0.76	0.73
spherical beta model								
Abell 697	2.74 ± 0.24	72 ± 8	0.19 ± 0.02	-	-	1397/1119	0.00	0.00
Abell 1835	2.46 ± 0.31	63 ± 8	0.17 ± 0.02	-	-	1008/947	0.08	0.08
MS 0015.9+1609	2.54 ± 0.29	80 ± 11	0.40 ± 0.05	-	-	1099/1119	0.66	0.61
MS 0451.6-0305	2.92 ± 0.24	53 ± 7	0.24 ± 0.03	-	-	1222/1119	0.02	0.02
MS 1054.4-0321	2.13 ± 0.22	56 ± 10	0.40 ± 0.07	-	-	1085/1119	0.76	0.76

NOTE. — Table of the best-fit parameters and 1σ uncertainties for our beta model fits with the power law exponent β set to the best-fit value found in P10 (0.86). From left to right the columns give the normalization of the beta profile, y_0 , the core radius of the major axis, r_c , the relative value of the core radius, r_c/r_{500} , the ellipticity, ϵ , the position angle of the major axis in degrees east of north, θ , the χ^2 and DOF for the fit, and the goodness of fit quantified by the probability to exceed the given χ^2/DOF based on the standard χ^2 probability distribution function and also empirically by the fraction of our 1000 noise realizations that produce a larger χ^2 value when a model cluster is added to them (see Section 6.2). The values of r_c/r_{500} for the spherical fits can be compared to the nominal value of 0.20 given in P10 based on spherical fits of SPT SZ data. See Section 6.2 for a description of how the parameter uncertainties are calculated. Note that we have included the 4.3% uncertainty in our flux calibration in the error estimates for y_0 .

All of these clusters have been studied extensively at a wide range of wavelengths, providing us with a large number of published results to compare our model fit parameters to. In general, our results agree well with those found from previous studies. In particular, when we fit a spherical beta model to our data using the values of β given in B06, which were determined using *Chandra* X-ray data and 30 GHz interferometric SZ data, our best-fit values for y_0 agree quite well, with the exception of Abell 697 (see Table 4). The best-fit values we find for r_c are also consistent with those determined in B06, with the exception of Abell 1835 and MS 0451.6-0305. Additionally, the ellipticity and orientation of our

elliptical fits are in general consistent with previously published results (Maughan et al. 2008; Donahue et al. 2003; De Filippis et al. 2005; Piffaretti et al. 2003; Girardi et al. 2006; McNamara et al. 2006; Schmidt et al. 2001; Neumann and Arnaud 2000). Finally, the best-fit concentration parameters from our Nagai model fits to three of the five clusters are consistent with those found from X-ray data (Arnaud et al. 2009); MS 0015.9+1609 and MS 1054.4-0321 have significantly lower values of c_{500} . We describe each cluster in detail below:

Abell 697: We find that Abell 697 has a significant ellipticity, and it is not well described by either a

TABLE 4
BETA MODEL FIT PARAMETERS COMPARED TO OVRO/BIMA/*Chandra* RESULTS

cluster	y_0 (10^{-4})		β	r_c (arcsec)		δRA	δdec
	Bolocam	OV/BI/ <i>Ch</i>		Bolocam	OV/BI/ <i>Ch</i>		
Abell 697	3.63 ± 0.31	$2.29^{+0.23}_{-0.24}$	0.607	49 ± 6	$43.2^{+2.1}_{-2.0}$	-6.2 ± 4.2	-14.0 ± 4.6
Abell 1835	2.95 ± 0.37	$3.19^{+0.19}_{-0.21}$	0.670	49 ± 6	$32.4^{+1.4}_{-1.1}$	-8.2 ± 4.4	1.5 ± 5.0
MS 0015.9+1609	2.80 ± 0.31	$2.55^{+0.15}_{-0.15}$	0.744	69 ± 10	$42.9^{+2.6}_{-2.4}$	18.2 ± 5.2	5.3 ± 4.7
MS 0451.6-0305	3.05 ± 0.25	$2.72^{+0.15}_{-0.13}$	0.795	48 ± 6	$36.0^{+1.9}_{-1.6}$	14.2 ± 4.6	7.9 ± 4.2
MS 1054.4-0321	1.92 ± 0.20	$2.09^{+0.17}_{-0.17}$	1.083	70 ± 12	$70.5^{+6.5}_{-6.9}$	-1.0 ± 4.4	-1.5 ± 4.6

NOTE. — Table of the best-fit parameters and 1σ uncertainties when we fit a spherical beta model to our data using the value of β found by B06 using OVRO/BIMA and *Chandra* data (in contrast to our nominal beta model fits with $\beta = 0.86$). From left to right the columns give our best-fit values of y_0 , the B06 best-fit values of y_0 , the value of β , our best-fit values of r_c , the B06 best-fit values of r_c , and the RA and dec offsets of the centroids of our best-fit models compared to the X-ray centroids of the B06 fits. Compared to B06, we find a significantly larger value of y_0 for Abell 697, and we find significantly larger values of r_c for Abell 1835 and MS 0015.9+1609. We also find small, but measurable, centroid offsets for all of the clusters other than MS 1054.4-0321.

beta model or a Nagai model. The poor model fits result from the cluster appearing significantly extended in the SW direction, and extremely compact in the NE direction. Abell 697 is the only cluster in our sample that is not adequately described by the models. The ellipticity we find for Abell 697, $\epsilon = 0.37 \pm 0.05$, is roughly consistent with the ellipticity of $\simeq 0.25$ found from X-ray data (De Filippis et al. 2005; Maughan et al. 2008; Girardi et al. 2006). We find a position angle of -24 deg for Abell 697, which is similar to the value of -16 deg found by Girardi et al. (2006), but somewhat misaligned to the position angle of 16 deg found by De Filippis et al. (2005).

Abell 1835: We detect an ellipticity in our image of Abell 1835, and we find that it is well described by either an elliptical beta or Nagai model. Our best-fit spherical Nagai model parameters with $\mathcal{A} = 0.9$, $\mathcal{B} = 5.0$, and $\mathcal{C} = 0.4$ ($p_0 = 11.1 \pm 2.6 \times 10^{-11}$ erg/cm³, $r_s = 4.6 \pm 1.1$ arcmin) are consistent with the values found in Mroczkowski et al. (2009) ($p_0 = 13.6 \times 10^{-11}$ erg/cm³, $r_s = 4.3$ arcmin) using a combination of SZA SZ data and *Chandra* X-ray data. X-ray measurements find an ellipticity of $0.1 - 0.2$ for Abell 1835 (De Filippis et al. 2005; McNamara et al. 2006; Schmidt et al. 2001), consistent with the value of $\epsilon = 0.27 \pm 0.07$ we find with Bolocam. We find a position angle of -16 deg for Abell 697, which is similar to the values of 7 , -20 , and -30 deg found by De Filippis et al. (2005), McNamara et al. (2006), and Schmidt et al. (2001).

MS 0015.9+1609: MS 0015.9+1609 appears to be elliptical in our image, and it is well described by either a spherical or elliptical model. As with Abell 697 and Abell 1835, X-ray data favor slightly lower ellipticities, $\epsilon \lesssim 0.20$, compared to what we find with Bolocam, $\epsilon = 0.24 \pm 0.08$ (De Filippis et al. 2005; Maughan et al. 2008; Piffaretti et al. 2003). We find a position angle of 68 deg for MS 0015.9+1609, fairly close to the value of 47 deg found by Piffaretti et al. (2003), but almost orthogonal to the value of -49 deg found by

De Filippis et al. (2005).

MS 0451.6-0305: MS 0451.6-0305 also appears to be elliptical in our image and is adequately described by either an elliptical beta or Nagai model. We find an ellipticity of $\epsilon = 0.26 \pm 0.06$ for MS 0451.6-0305, in excellent agreement with ellipticities determined using X-ray data (De Filippis et al. 2005; Donahue et al. 2003). Additionally, our best-fit position angle of 85 deg agrees well with the value of 84 deg found by De Filippis et al. (2005) and the value of -75 deg found by Donahue et al. (2003).

MS 1054.4-0321: Our image of MS 1054.4-0321 shows no evidence for ellipticity, and it is well described by either an elliptical or spherical model. Although MS 1054.4-321 does not appear to be elliptical in our data, X-ray data show a clear ellipticity oriented along the east-west direction (Neumann and Arnaud 2000; Jelteima et al. 2001). However, our non-detection of an ellipticity, $\epsilon = 0.09 \pm 0.07$, is only marginally inconsistent with the X-ray value determined by Neumann and Arnaud (2000), $\epsilon = 0.29$.

SDS1: We have attempted to fit cluster models to the SDS1 map, but we find best-fit amplitudes that are consistent with 0 and best-fit scale radii that are large compared to the size of our images (*i.e.*, scale radii that are large enough to produce profiles that are approximately constant over the entire image).

5. MODEL-INDEPENDENT IMAGES AND Y_{SZ} ESTIMATES

Rather than using models, which at best provide an adequate description of what clusters look like on average, we have chosen to derive observable quantities from our images in a quasi-model-independent way. In Section 3.3 we described how we calculate a unique transfer function for each cluster to quantify the effects of our noise filtering. In the Fourier space of our images, these transfer functions are a set of two-dimensional complex numbers that describe how an input cluster image is filtered as a function of two-dimensional Fourier mode. We obtain an unfiltered, or deconvolved, image of the cluster by Fourier transforming our image, dividing by the two-dimensional

complex transfer function, and then Fourier transforming the result back to image space⁷. At the largest scales in our map, the transfer function has a magnitude of $\simeq 0.2$ (see Figure 3), resulting in a numerically stable, but significant, amplification of the large scale noise. In particular, the residual atmospheric noise and primary CMB fluctuations, which had been filtered to be approximately white, produce a significant low-frequency noise component in our deconvolved images. We estimate the noise in our deconvolved images by deconvolving each of the 1000 noise realizations for each cluster. Since the off-diagonal elements of the noise covariance matrix are significant due to the low-frequency noise, we estimate all of our measurement uncertainties from the standard deviation of measuring the same quantity in each of our 1000 deconvolved noise realizations (see below and Section 6.2). Note that most of the measurement uncertainties in our processed (*i.e.*, filtered) images are computed in the same way, even though their noise covariance matrix is approximately diagonal.

By deconvolving the two-dimensional transfer function of our data processing we obtain unbiased cluster images, modulo smoothing with our PSF and the unconstrained DC signal level. Although the transfer function was computed using the best-fit-elliptical Nagai model, and is therefore somewhat model dependent, the dependence is negligible other than the determination of the DC signal offset of the image (see Section 6.1). We do not attempt to recover the information lost due to smoothing by our PSF, but we use the value of δT found from our elliptical Nagai model fits to restore the correct DC signal level to our images. Due to uncertainties in the model itself, especially at large radii where there is little or no observational data, along with cluster-to-cluster deviations from the model, this does introduce a non-negligible model-based bias in our images (the typical model uncertainty in the DC signal offset is $5 - 10 \mu\text{K}_{\text{CMB}}$, see Section 6.1). However, we emphasize that this bias only affects the DC signal level of the images; the shapes of the cluster profiles are essentially model-independent.

We have computed a model-independent value for Y_{500} from these deconvolved images, which is the integrated y within r_{500} (*i.e.*, the cylindrical Y_{500} rather than the spherical Y_{500} , see Table 5). As mentioned above, since our assumption that the noise covariance matrix is diagonal fails for the deconvolved images, we estimate the uncertainty in our estimate of Y_{SZ} via the scatter among the Y_{SZ} values determined from each of our noise realizations. As an example of the amount of low-frequency noise present in our deconvolved images on the scale of r_{500} , note that the measurement uncertainty on Y_{500} is approximately 10 times larger than it would be if the noise was white. For the five clusters in our sample, we are able to determine Y_{SZ} with an uncertainty of $\simeq 10\%$, limited mainly by systematics in determining the DC sig-

nal offset and flux calibration.

We examine the self-similar scaling that is expected between Y_{SZ} and the total cluster mass using the relation given in Bonamente et al. (2008),

$$Y_{SZ} D_A^2 E(z)^{-2/3} \propto f_{gas}^{-2/3} M_{gas}^{5/3},$$

where D_A is the angular diameter distance, $E(z) = \sqrt{\Omega_m(1+z)^3 + \Omega_\Lambda}$, and we have assumed M_{gas} is a good proxy for the total cluster mass (Allen et al. 2008; Mantz et al. 2010a). The scatter in this relation is expected to be $\lesssim 10\%$ (Kravtsov et al. 2006), and current measurements are roughly consistent with this prediction (Morandi et al. 2007; Bonamente et al. 2008; Marrone et al. 2009; Plagge et al. 2010; Huang et al. 2010; Andersson et al. 2010). Given our small sample, we do not attempt to constrain the intrinsic scatter in the $Y - M$ relation, but we follow the formalism of Marrone et al. (2009) and P10 to fit a logarithmic scaling of the form $\mathcal{Y} = a + b\mathcal{X}$ with the intrinsic scatter set to 10%. For the $Y_{500} - M_{gas,500}$ relation we find best-fit values of $a = -5.46 \pm 0.84$ and $b = 1.63 \pm 0.71$, consistent with the self-similar prediction of $b = 5/3$. The overall scatter of our data about the fit is 13%, consistent with an intrinsic scatter of $\simeq 10\%$ given our $\simeq 10\%$ uncertainty on Y_{SZ} (see Figure 6).

Additionally, our results are consistent with $Y_{SZ} - M_{gas}$ scaling relations measured by other groups. For example, our results using model-independent Y_{SZ} estimates from Bolocam and M_{gas} estimates from *Chandra* within r_{500} agree well with the results in P10 using Y_{SZ} estimates from the SPT best-fit beta model and M_{gas} estimates primarily from *XMM-Newton* ($a = -5.73 \pm 0.43$ and $b = 2.12 \pm 0.45$ within r_{500} and $a = -5.92 \pm 0.41$ and $b = 1.97 \pm 0.44$ within r_{2500}). The results in Bonamente et al. (2008), using beta model fits to 30 GHz OVRO/BIMA SZ data and *Chandra* X-ray data within r_{2500} , also match our results quite well ($a = -5.22 \pm 1.77$ and $b = 1.41 \pm 0.13$).

6. TESTS FOR SYSTEMATIC ERRORS

We are primarily concerned with two types of systematic errors that may occur in our analysis: those caused by our (minimal) use of a cluster model, specifically an elliptical Nagai model, and those caused by characteristics of our noise that are not properly accounted for in our analysis. We have run extensive tests to quantify the level of systematic error we can expect from each of these two sources. The details of these tests are described below. In the end, we find that the amount of systematic error in our images is negligible, with the exception of the estimation of the DC signal offset in our images using the Nagai model.

6.1. Model dependence of results

Since we compute the transfer function for each cluster using the best-fit elliptical Nagai model for that cluster, our deconvolved images necessarily have some model dependence. In order to quantify the amount of model dependence, we have computed transfer functions for a range of elliptical Nagai models for one of the clusters in our sample, MS 0451.6-0305. Relative to the best-fit model, we have varied the scale radius, r_s , the ellipticity, ϵ , the position angle, θ , and the centroid location, δRA

⁷ This method can be compared to the deconvolution method employed by APEX-SZ for their analysis of Abell 2163 and Abell 2204 (Nord et al. 2009; Basu et al. 2010). They first determine what a point-like object looks like in their image after being filtered. Next, they fit this filtered point-source image to the map pixel with the largest S/N and subtract it from the image. The process is repeated until the map is consistent with noise; the sum of all the unfiltered point-like images removed from the map gives the deconvolved cluster image.

TABLE 5
MODEL-INDEPENDENT Y_{500} ESTIMATES

cluster	Y_{500}	JK noise σ_Y	CMB/PS σ_Y	map DC signal σ_Y	flux cal. σ_Y
Abell 697	59.2 ± 6.3	1.2	0.5	5.6	2.5
Abell 1835	47.5 ± 4.9	1.3	0.5	4.3	2.0
MS 0015.9+1609	23.3 ± 2.2	1.6	0.6	0.9	1.0
MS 0451.6-0305	24.7 ± 2.0	1.2	0.6	0.9	1.1
MS 1054.4-0321	8.8 ± 1.0	0.8	0.4	0.2	0.4

NOTE. — Model independent estimates of Y_{500} , in units of 10^{-11} ster, along with the associated uncertainties. From left to right the columns give the value and total uncertainty of our estimate of Y_{500} , the uncertainty due to our jackknife noise model (*i.e.*, excluding CMB and point sources), the uncertainty due to CMB and point sources, the uncertainty in the DC signal level of the map (see Section 6.1), and the uncertainty in our flux calibration. Note that the jackknife noise estimate is dominated by large angular-scale residual atmospheric fluctuations; the noise on beam-size scales is negligible.

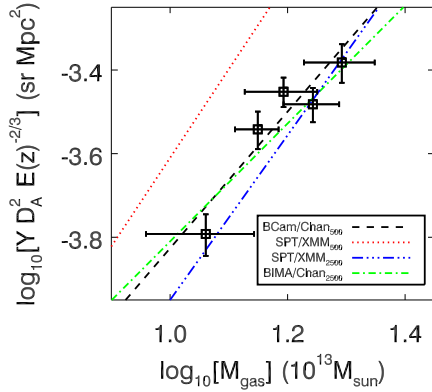


FIG. 6.— Scaling relation between Y_{SZ} and M_{gas} for the five clusters in our sample. The black squares give the Bolocam model-independent cylindrical Y_{500} estimates and *Chandra* $M_{gas,500}$ estimates (see Table 1), and the black dashed line represents the best fit to these data. We also show fits of a similar type obtained by various authors: red dashed: SPT beta-model-derived Y_{500} vs. $M_{gas,500}$, primarily obtained from *XMM-Newton* data (P10); solid blue: same, but within r_{2500} ; dot-dashed green: OVRO/BIMA beta-model-derived Y_{2500} vs. $M_{gas,2500}$ obtained from *Chandra* data (Bonamente et al. 2008). The difference between the red-dashed line and our data is likely caused by systematic differences between model-derived and model-independent estimates of Y_{500} ^a. The scatter of our data relative to our best fit is 13%, consistent with the expected intrinsic scatter of $\simeq 10\%$ given our $\simeq 10\%$ uncertainty on Y_{500} .

^a P10 calculated both model-derived and model-independent estimates of Y_{SZ} for the 15 clusters in their sample. Within a radius of r_{2500} , the two estimates of Y_{2500} are on average consistent with each other. However, the P10 model-derived estimates of Y_{500} are on average a factor of 1.5 larger than the model-independent estimates for the 10 clusters used to determine the $Y_{SZ} - M_{gas}$ scaling relation. As a result, the P10 model-derived scaling relation for $Y_{500} - M_{gas,500}$ will be systematically higher by $\log_{10}(1.5) \simeq 0.2$ compared to a model-independent scaling relation.

and δdec , by increasing and decreasing each parameter individually by its 1σ uncertainty⁸. We then deconvolved our processed map of MS 0451.6-0305 using the transfer function computed from each model and subtracted the resulting map from the one produced using the transfer

⁸ The power law slopes (\mathcal{A} , \mathcal{B} , and \mathcal{C}) were held fixed for all of our model fits. Due to the large degeneracy between these values and r_s , we have effectively included variations in the power law slopes by varying the value of r_s .

function for the best-fit model. In each case, the residual map was approximately white, with an RMS of 1.5, 0.6, and $0.5 \mu\text{K}_{CMB}$ for variations in r_s and ϵ , θ , and δRA and δdec , respectively. Since the typical noise RMS of our deconvolved maps is $\simeq 10 \mu\text{K}_{CMB}$, the additional RMS introduced by our uncertainty in determining the model used for calculating a transfer function is quasi-negligible. Note that the best-fit elliptical Nagai model will not provide an exact description of a real cluster. However, the elliptical Nagai model does provide an adequate description of four of the five clusters we have observed, indicating that the difference between the true cluster profile and the model profile is in general less than our noise. Therefore, the artifacts in our deconvolved map produced by using a model to describe the cluster will be smaller than the artifacts produced by our measurement uncertainty on the best-fit model.

Additionally, we created a deconvolved map of MS 0451.6-0305 using the transfer function for a point-like source. The resulting profile is significantly different from the profile obtained using the transfer function for the best-fit Nagai model, indicating that the naive calculation of a transfer function using a point source is inadequate. Compared to using the transfer function calculated from the best-fit elliptical Nagai model, the peak decrement is reduced by $\simeq 50 \mu\text{K}_{CMB}$, while the magnitude of the SZ signal at the edge of the map is increased by $\simeq 50 \mu\text{K}_{CMB}$ (*i.e.*, the deconvolved cluster image from a point-source transfer function is systematically broader).

As described in Section 4, we use the best-fit elliptical Nagai model to determine the DC signal level in our maps since its value is unconstrained by our data. The measurement uncertainty in the value of the DC signal is small, $< 1 \mu\text{K}_{CMB}$, but there is a large amount of uncertainty in the model at large radii. Based on the results from Borgani et al. (2004), N07, and Piffaretti and Valdarnini (2008) presented in Arnaud et al. (2009), the RMS scatter in the pressure profiles from cluster to cluster in simulations is $\lesssim 25\%$. Therefore, we include an additional 25% systematic uncertainty on the DC signal that we add to the deconvolved map. Specifically, we estimate that the model uncertainty in the DC signal level of our map is 25% of the signal level at the edge of the map.

6.2. Noise characteristics

As mentioned in Section 3, we make the approximation that the noise covariance matrix is diagonal in our processed maps (*i.e.*, there are no noise correlations between pixels). Although fluctuations in both the atmospheric emission and the CMB are correlated over many pixels, the high-pass filter we apply to our data timestreams eliminates these correlations within our ability to measure them. To test for noise correlations, we added processed cluster images of the best-fit models to the 1000 noise realizations for each cluster (*i.e.*, for a given cluster we separately added each of the four best-fit cluster models from Tables 2 and 3 to each of the 1000 noise realizations). We then fit a model of the same type (*e.g.*, if we added the best-fit elliptical Nagai model to the noise realization, then we fit an elliptical Nagai model to the cluster-model-plus-noise map) to each of these model-cluster-plus-noise maps and examined the distribution of χ^2 values for these fits. For all five clusters, we found that the distribution of χ^2 values matched the predicted χ^2 distribution obtained from the diagonal noise covariance matrix⁹. As an example, the fit quality of our measured χ^2 distribution for the elliptical-Nagai-model-plus-noise realizations to the predicted χ^2 distribution, quantified by a PTE, is 0.58, 0.02, 0.08, 0.66, and 0.21 for Abell 697, Abell 1835, MS 0015.9+1609, MS 0451.6-0305, and MS 1054.4+321. (see Figure 7). Therefore, we conclude that there is a negligible amount of correlated noise in our processed images and our assumption that the noise covariance matrix is diagonal is valid. Furthermore, we have estimated all of our parameter uncertainties (p_0 , r_s , etc.) directly from the distribution of values calculated from our noise realizations. Consequently, any failure of our assumption that the covariance matrix is diagonal for the processed images will only affect the pixel-weighting and χ^2 values for our model fits.

However, when we perform the same test of fitting a model to our model-cluster-plus-noise maps using noise realizations that have been deconvolved with our transfer function, the result is significantly different. The distribution of χ^2 values calculated from our deconvolved noise realizations is significantly broader than the predicted distribution based on uncorrelated noise (see Figure 7). This result is not surprising since the deconvolution enhances the large-scale signals in the images, including residual atmospheric noise and CMB fluctuations. Since the noise in the deconvolved images is significantly spatially correlated, our assumption that the noise covariance matrix is diagonal fails. Therefore, we estimate the uncertainties for the deconvolved images using the spread in values for the noise realizations rather than from the diagonal elements of the noise covariance matrix (*e.g.*, the uncertainties in the radial profiles are determined from the RMS spread in the radial profiles of the noise realizations). This is the same technique used by Nord et al. (2009) and Basu et al. (2010) to analyze APEX-SZ data.

The model fits to the model-cluster-plus-noise realiza-

tions also provide us with estimates of the uncertainties and biases associated with our model-parameter fitting. Specifically, we obtain 1000 best-fit values for each parameter; the standard deviation of these values then gives the uncertainty on our estimate of that parameter in our actual data map. These uncertainties are given in Tables 2 and 3. In addition, if our parameter estimation algorithm is free from biases, then we should, on average, recover the parameters of the input model that was added to the noise realizations. In practice, we find a small, but measurable, bias in our estimates of the pressure normalization and scale radius in our fits; the bias is typically $\lesssim 10\%$ of the uncertainty on each parameter. We find no measurable bias in our estimates of the other fit parameters.

Additionally, we have used our signal-free SDS1 maps to further verify our model-fitting procedure and to search for any components of the noise that have not been included in our noise estimate. First, we inserted model clusters into the SDS1 data timestreams based on the best-fit elliptical Nagai profile for each of the five clusters in our sample. These data were then processed and an elliptical Nagai model was fit to each resulting image. In each fit, there are 6 free parameters (p_0 , r_s , ϵ , θ , δRA , and δdec), giving us a total of 30 fit parameters for the 5 model clusters. Of these 30 fit parameters, 17 (57%) are within 1σ of the input value, 26 (87%) are within 2σ of the input value, and all 30 are within 3σ of the input value; these results indicate that our model fitting and parameter error estimation are working properly. Additionally, we obtain a reasonable goodness of fit for the models using these best-fit parameters, quantified by a PTE $\simeq 0.8$, providing further evidence that there is no significant noise in the data that has not been included in our noise estimate. Note that since the five cluster model profiles are fairly similar, we obtain comparable PTEs for all five profiles.

7. SUMMARY

We have presented the first results from our program to image the SZ effect in galaxy clusters with Bolocam. These images have a beam-smoothed RMS of $\simeq 10 \mu K_{CMB}$, and a resolution of 58 arcsec. Given this noise level, we are able to measure SZ signal in radial profiles to approximately the edge of our maps, which corresponds to 6-7 arcmin or 1 – 2 times r_{500} . In order to subtract noise from atmospheric fluctuations, we effectively high-pass filter our cluster images. However, we are able to deconvolve the effects of this filter with biases that are negligible compared to our noise level, other than our recovery of the DC signal level. In fitting our images to spherical and elliptical beta and Nagai models, we find no preference between the beta and Nagai models due to the degeneracy between these models over the angular range to which our data are sensitive, but our data do show a definitive preference for elliptical models over spherical models. The weighted mean ellipticity of the five clusters is $\epsilon = 0.27 \pm 0.03$, consistent with results from X-ray data. Additionally, the best-fit model parameters we determine from our data are consistent with those found from previous X-ray and SZ measurements. We have also obtained model-independent estimates of Y_{SZ} , and we find scaling relations between Y_{SZ} and cluster mass that are consistent with self-similar predictions,

⁹ We have fit for N_{params} free parameters in our fits to both the actual data and the noise realizations, with $N_{params} = 5$ or 7 for the spherical or elliptical fits. Therefore, the predicted χ^2 distribution is for $N_{pix} - N_{params}$ DOF, where N_{pix} is the number of map pixels.

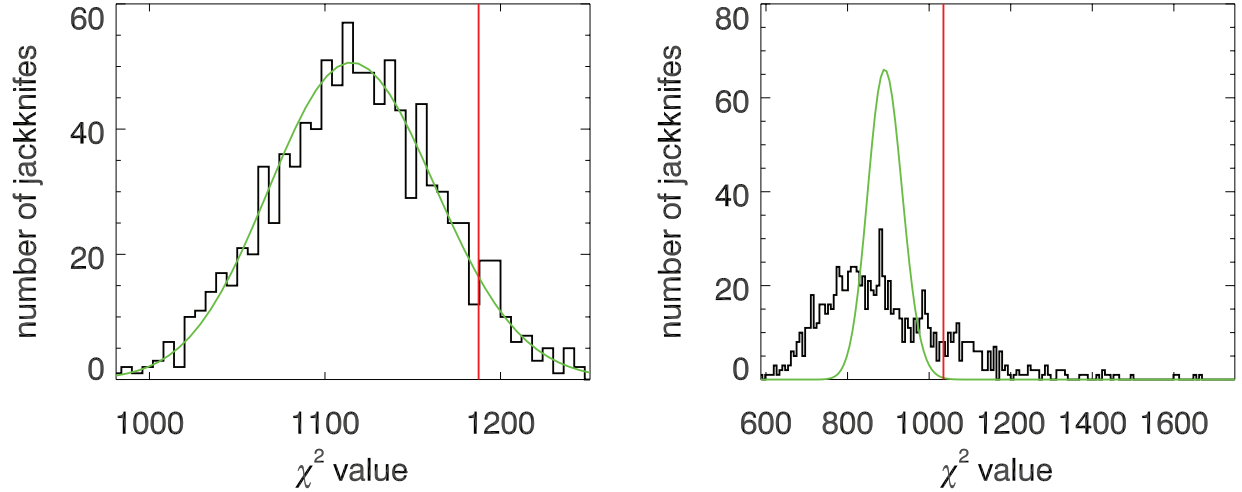


FIG. 7.— Histograms of the χ^2 value for 1000 separate noise realizations for MS 0451.6-0305, overplotted in green with the predicted distribution assuming the noise covariance matrix is diagonal (*i.e.*, there is no correlated noise). For each noise realization the best-fit elliptical Nagai model profile for MS 0451.6-0305 is added to the noise realization, an elliptical Nagai model is fit to this model-cluster-plus-noise realization, and the value of χ^2 is computed based on the assumption that the noise covariance matrix is diagonal. The vertical red line shows the value of χ^2 for the actual data for MS 0451.6-0305. The left histogram shows the processed data, and the right histogram shows the data for the deconvolved image. The predicted and actual χ^2 distributions for the processed data overlap, indicating that there are minimal correlations between map pixels. However, the actual χ^2 distribution for the deconvolved image data is much broader than the predicted distribution, indicating that there are significant noise correlations between map pixels in the deconvolved images.

with a scatter that is consistent with expectations for a $\simeq 10\%$ intrinsic scatter.

8. ACKNOWLEDGMENTS

We acknowledge the assistance of: Nicole Czakon, Tom Downes, and Seth Siegel, who have provided numerous comments and suggestions about the data analysis; the Bolocam instrument team: P. A. R. Ade, J. E. Aguirre, J. J. Bock, S. F. Edgington, J. Glenn, A. Goldin, S. R. Golwala, D. Haig, A. E. Lange, G. T. Laurent, P. D. Mauskopf, H. T. Nguyen, P. Rossinot, and J. Sayers; Matt Ferry, who helped collect the data for Abell 1835 and MS 1054.4-0321; the day crew and Hilo staff of the Caltech Submillimeter Observatory, who provided invaluable assistance during commissioning and data-taking for this survey data set; Daisuke Nagai for useful discussions about cluster modeling; Tony Mroczkowski for providing the best-fit pa-

rameters from his group's analysis of Abell 1835, useful comments about cluster modeling, and pointing out a typo in our original arxiv posting; the referee for several useful comments and suggestions; and Kathy Deniston, Barbara Wertz, and Diana Bisel, who provided effective administrative support at Caltech and in Hilo. Bolocam was constructed and commissioned using funds from NSF/AST-9618798, NSF/AST-0098737, NSF/AST-9980846, NSF/AST-0229008, and NSF/AST-0206158. JS was partially supported by a NASA Graduate Student Research Fellowship and a NASA Postdoctoral Program fellowship, SA and EP were partially supported by NSF grant AST-0649899, SA was partially supported by the USC WiSE postdoctoral fellowship and travel grants, and EP was partially supported by NASA grant NNX07AH59G and JPL-Planck subcontract 1290790.

Facilities: CSO.

REFERENCES

- Allen, S. et al., 2003, MNRAS, 342, 287
 Allen, S. et al., 2003, MNRAS, 346, 593
 Allen, S. et al., 2008, MNRAS, 383, 879
 Ameglio, S. et al., 2007, MNRAS, 382, 397
 Ameglio, S. et al., 2010, in prep
 Andersson, K. et al., astro-ph/1006.3068
 Arnaud, M. et al., 2010, A&A, 517, A92
 Bahcall, N. et al., 1997, ApJ, 485, L53
 Basu, K. et al., 2010, A&A, 519, A29
 Bevington, P. and Robinson, D., 1992, Data Reduction and Error Analysis for the Physical Sciences (2nd ed)
 Bonamente, M. et al., 2006, ApJ, 647, 25
 Bonamente, M. et al., 2008, ApJ, 675, 106
 Borgani, S. et al., 2001, ApJ, 561, 13
 Borgani, S. et al., 2004, MNRAS, 348, 1078
 Carlstrom, J. et al., 2002, ARA&A, 40, 643
 Cavagnolo, K. et al., 2008, ApJ, 682, 821
 Cavaliere, A. and Fusco-Femiano, R., 1976, A&A, 49, 137
 Cavaliere, A. and Fusco-Femiano, R., 1978, A&A, 70, 677
 Clowe, D. et al., 2006, ApJ, 648, L109
 Cooray, A. et al., 1998, ApJ, 115, 1388
 Croston, J. et al., 2008, A&A, 487, 431
 Culverhouse, T. et al., 2010, ApJ, 723, L78
 De Filippis, E. et al., 2005, ApJ, 625, 108
 Diaferio, A. and Ostorero, L., 2009, MNRAS, 393, 215
 Donahue, M. et al., 2003, ApJ, 598, 190
 Ettori, S. et al., 2009, A&A, 501, 61
 Finoguenov, A. et al., 2010, MNRAS, 403, 2063
 Girardi, M. et al., 2006, A&A, 455, 45
 Glenn, J. et al., 1998, Proc. SPIE, 3357, 326
 Gonzalez, A. et al., 2007, ApJ, 666, 147
 Gralla, M. et al., 2010, astro-ph/1010.6011
 Griffin, M. et al., 1986, Icarus, 65, 244
 Griffin, M. and Orton, G., 1993, Icarus, 105, 537
 Haig, D. et al., 2004, Proc. SPIE, 5498, 78
 Haiman, Z. et al., 2001, MNRAS, 395, 657
 Hall, N. et al., 2010, ApJ, 718, 632
 Hallman, E. et al., 2007, ApJ, 665, 911
 Halverson, N. et al., 2009, ApJ, 701, 42
 Hao, J. et al., 2010, astro-ph/1010.5503

- Hill, R., et al., 2009, *ApJS*, 180, 246
 Holder, G. et al., 2000, *ApJ*, 544, 629
 Holder, G. et al., 2001, *ApJ*, 560, L111
 Huang, C.-W. et al., 2010, *ApJ*, 716, 758
 Itoh, N. et al., 1998, *ApJ*, 502, 7
 Ivison, R. et al., 2000, *MNRAS*, 315, 209
 Jee, M. et al., 2005, *ApJ*, 616, 46
 Jeltema, T. et al., 2001, *ApJ*, 562, 124
 Kaiser, N., 1986, *MNRAS*, 222, 323
 Korngut, P. et al., 2010, *astro-ph/1010.5494*
 Kovacs, A. et al., 2006, *ApJ*, 650, 592
 Kravtsov, A. et al., 2006, *ApJ*, 650, 128
 Lin, Y.-T. et al., 2009, *ApJ*, 694, 992
 Lo Verde, M. et al., 2008, *J. Cosmo. Astrop. Phys.* 04, 014
 Lueker, M. et al., 2010, *ApJ*, 719, 1045
 Mantz, A. et al., 2010, *MNRAS*, 406, 1759
 Mantz, A. et al., 2010, *MNRAS*, 406, 1773
 Marrone, D. et al., 2009, *ApJ*, 701, L114
 Martino, M. et al., 2009, *Phys. Rev. D*, 79, 084013
 Maughan, B. et al., 2008, *ApJS*, 174, 117
 Mason, B. et al., 2010, *ApJ*, 716, 701
 McNamara, B. et al., 2006, *ApJ*, 648, 164
 Menanteau, F. et al., 2010, *astro-ph/1002.2226*
 Menanteau, F. et al., 2010, *ApJ*, 723, 1523
 Moffat, J. and Toth, V., 2010, *astro-ph/1005.2685*
 Morandi, A. et al., 2007, *MNRAS*, 379, 518
 Mroczkowski et al., 2009, *ApJ*, 694, 1034
 Muhleman, D. and Berge, G., 1991, *Icarus*, 92, 263
 Nagai, D. et al., 2007, *ApJ*, 668, 1
 Neumann, D. et al., 2000, *ApJ*, 542, 35
 Nord, M. et al., 2009, *A&A*, 506, 623
 Peterson, J. et al., 2001, *A&A*, 365, L104
 Pierpaoli, E. et al., 2001, *MNRAS*, 325, 77
 Pierpaoli, E. et al., *MNRAS*, 342, 163
 Pierpaoli, E., 2004, *Proc. Multiwavelength Cosmology Conf.*, 93
 Piffaretti, R. et al., 2003, *A&A*, 398, 41
 Piffaretti, R. and Valdarnini, R., 2008, *A&A*, 491, 71
 Pipino, A. and Pierpaoli, E., 2001, *MNRAS*, 404, 1603
 Pipino, A. et al., 2010, *astro-ph/1011.3017*
 Plagge, T. et al., 2010, *ApJ*, 716, 1118
 Rapetti, D. et al., 2010, *MNRAS*, 406, 1796
 Rines, K. and Diaferio, A., 2010, *ApJ*, 139, 580
 Rudy, D. et al., 1987, *Icarus*, 71, 159
 Sandell, G., 1994, *MNRAS*, 271, 75
 Sayers, J. et al., 2009, *ApJ*, 690, 1597
 Sayers, J. et al., 2010, *ApJ*, 708, 1674
 Schmidt, R. et al., 2001, *MNRAS*, 327, 1057
 Schmidt, F. et al., 2009, *Phys. Rev. D*, 80, 083505
 Serra, A. et al., 2010, *astro-ph/1011.0372*
 Spergel, D. et al., 2003, *ApJS*, 148, 175
 Sunyaev, R. and Zel'dovich, Y., 1972 *Comm. Astr. and Space Phys.*, 4, 173
 Szabo, T. et al., 2010, *astro-ph/1011.0249*
 Vanderlinde, K. et al., 2010, *ApJ*, 722, 1180
 Viana, P. and Liddle, A., 2009, *MNRAS*, 303, 535
 Vikhlinin, A. et al., 2006, *ApJ*, 640, 691
 Vikhlinin, A. et al., 2009, *ApJ*, 692, 1060
 Wright, E., 1976, *ApJ*, 210, 250
 Wu, X. et al., 2010, *J. Cosmo. Astrop. Phys.*, 06, 010
 Zemcov, M. et al., 2007, *MNRAS*, 376, 1073
 Zhang, Y.-Y et al., 2010, *astro-ph/1011.3018*

APPENDIX

This appendix includes images and radial profiles of the processed and deconvolved maps, an image of the processed residual map after subtracting the best-fit elliptical Nagai model, and an image of one of the 1000 noise estimates generated via jackknife realizations of the data and a model for the astronomical noise. We have smoothed all of the images using a Gaussian beam with a FWHM of 58 arcsec. A white dot representing the FWHM of the effective PSF for these beam-smoothed images is given in the lower left of each image. The solid white contour lines in the images represent a S/N of -2 , -4 , ..., and the dashed white contour lines represent a S/N of $+2$, $+4$, The deconvolved images contain a significant amount of noise that is correlated over large angular scales, along with a model-dependent DC signal offset, and we therefore do not display noise contours on the deconvolved images. The error bars on the radial profiles are estimated from the spread in radial profiles computed from our noise realizations, and therefore do include all of the large-angular-scale noise correlations (although they do not include the uncertainty in the DC signal level of the image). Note that the radial profile bins for the deconvolved images are correlated due to the large-angular-scale noise present in those images.

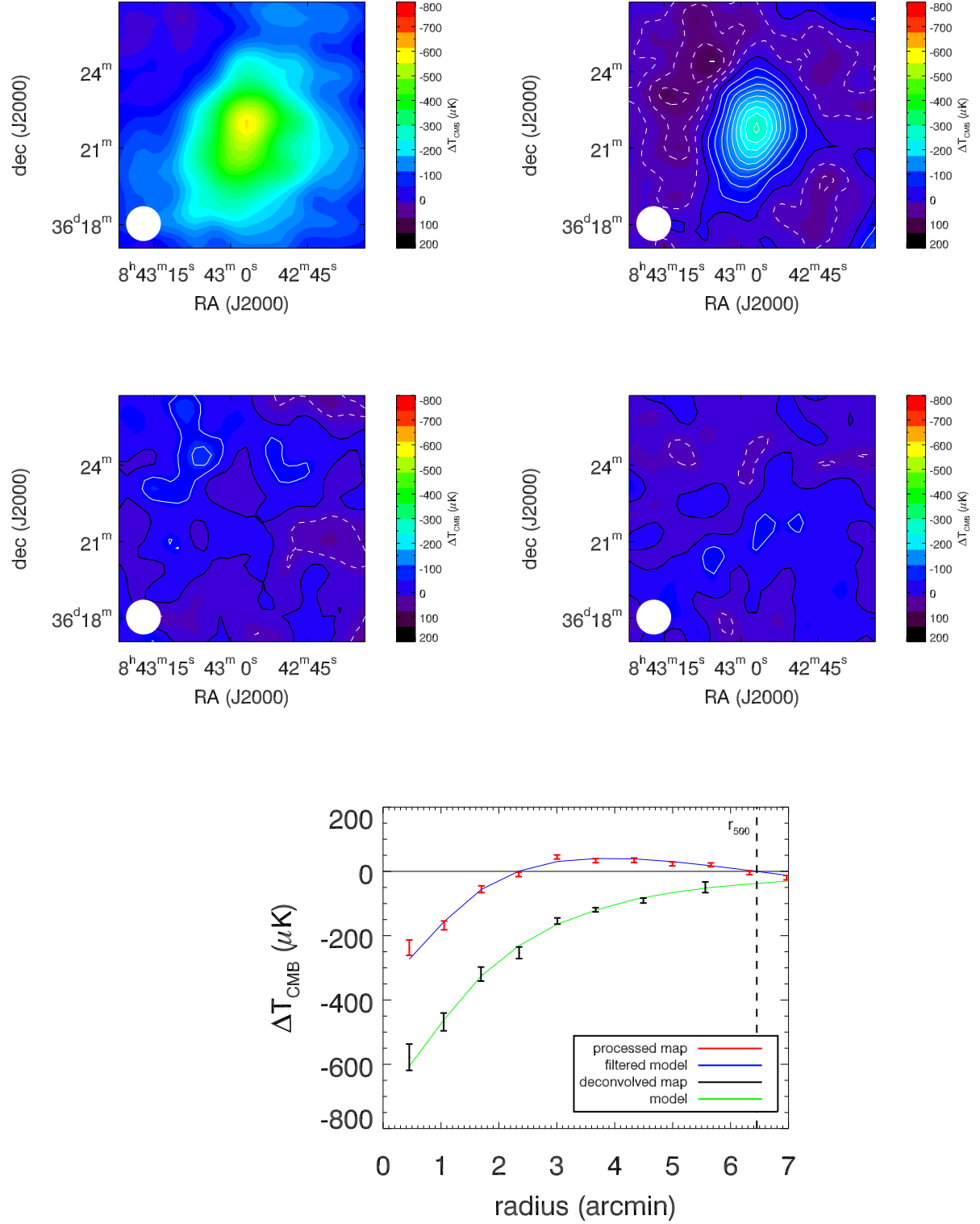


FIG. A1.— Abell 697; from left to right and top to bottom we show the deconvolved image of the cluster, the processed image of the cluster, the residual map between the processed image of the cluster and the best-fit elliptical Nagai model, one of the 1000 noise realizations for the processed data, and a binned radial profile. The contour lines represent a S/N of 2, 4, ...

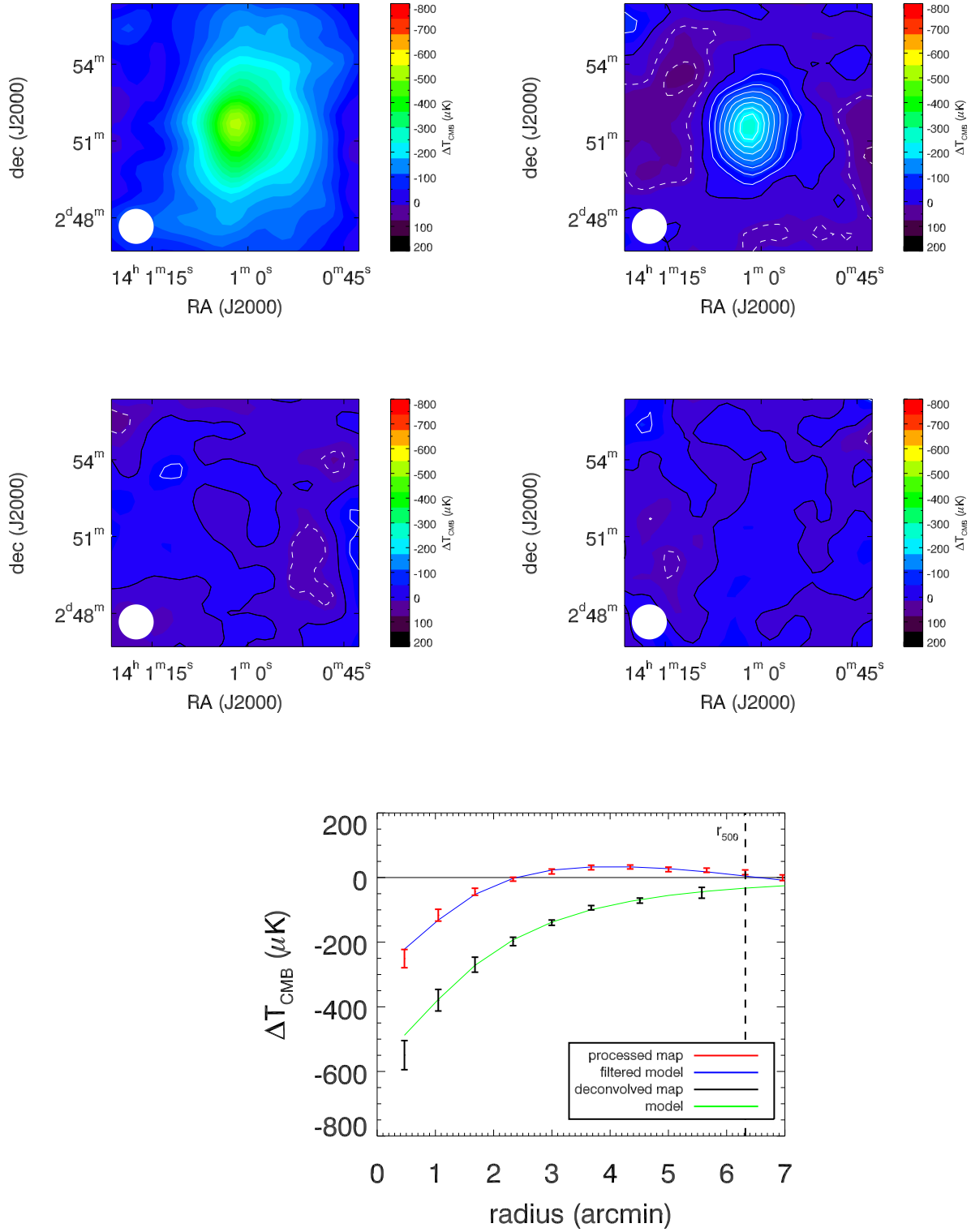


FIG. A2.— Abell 1835; from left to right and top to bottom we show the deconvolved image of the cluster, the processed image of the cluster, the residual map between the processed image of the cluster and the best-fit elliptical Nagai model, one of the 1000 noise realizations for the processed data, and a binned radial profile. The contour lines represent a S/N of 2, 4, ...

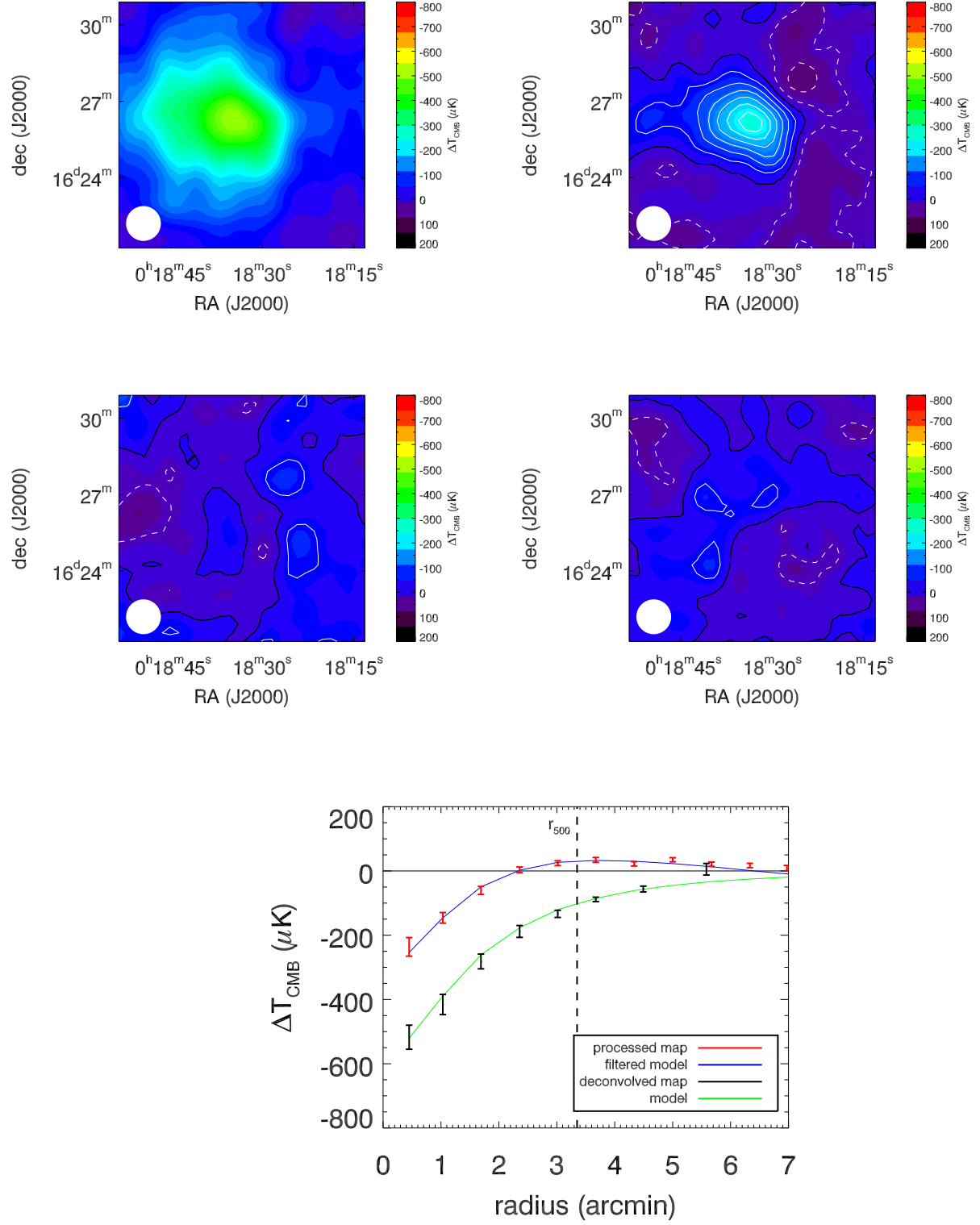


FIG. A3.— MS 0015.9+1609; from left to right and top to bottom we show the deconvolved image of the cluster, the processed image of the cluster, the residual map between the processed image of the cluster and the best-fit elliptical Nagai model, one of the 1000 noise realizations for the processed data, and a binned radial profile. The contour lines represent a S/N of 2, 4, ...

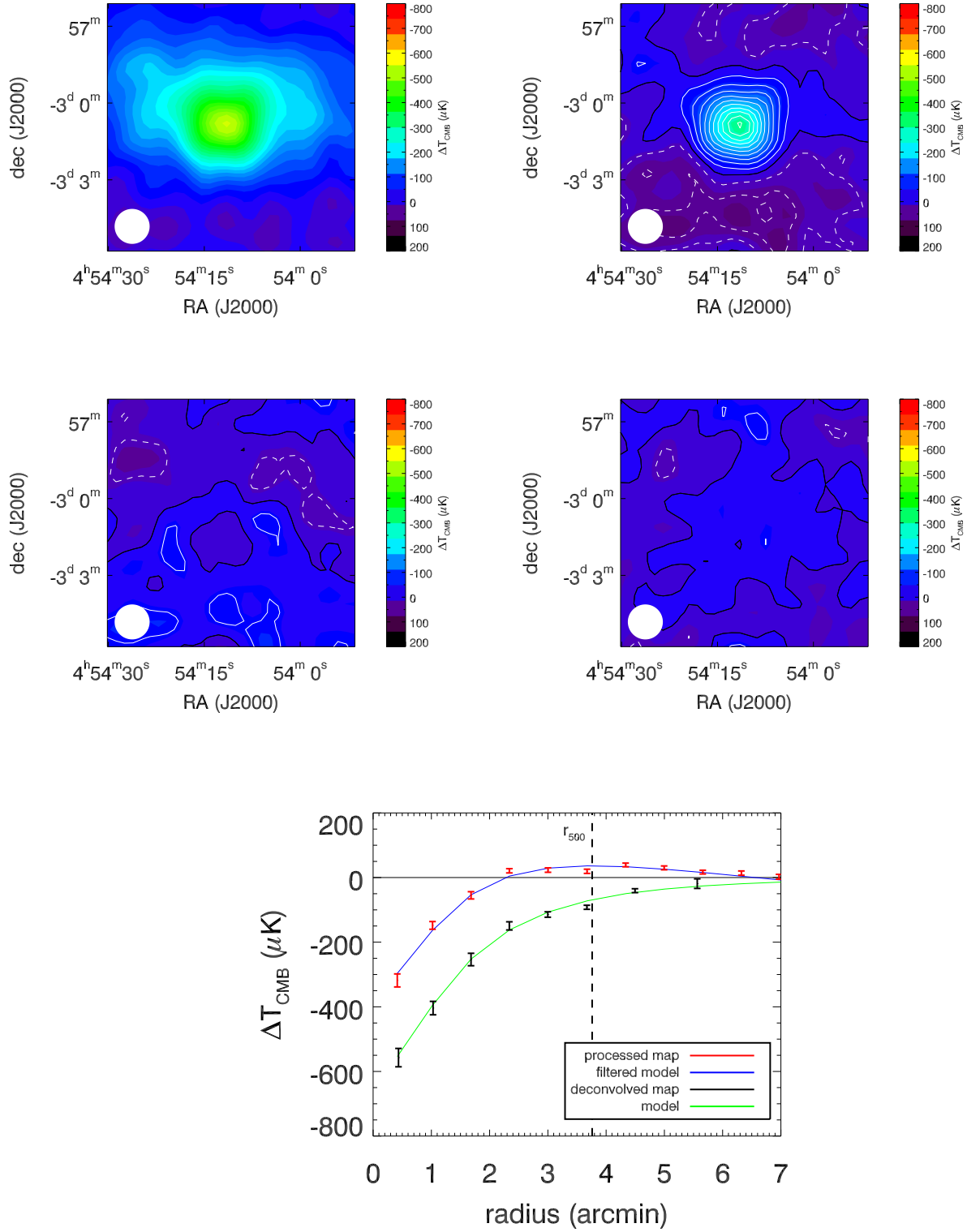


FIG. A4.— MS 0451.6-0305; from left to right and top to bottom we show the deconvolved image of the cluster, the processed image of the cluster, the residual map between the processed image of the cluster and the best-fit elliptical Nagai model, one of the 1000 noise realizations for the processed data, and a binned radial profile. The contour lines represent a S/N of 2, 4, ...

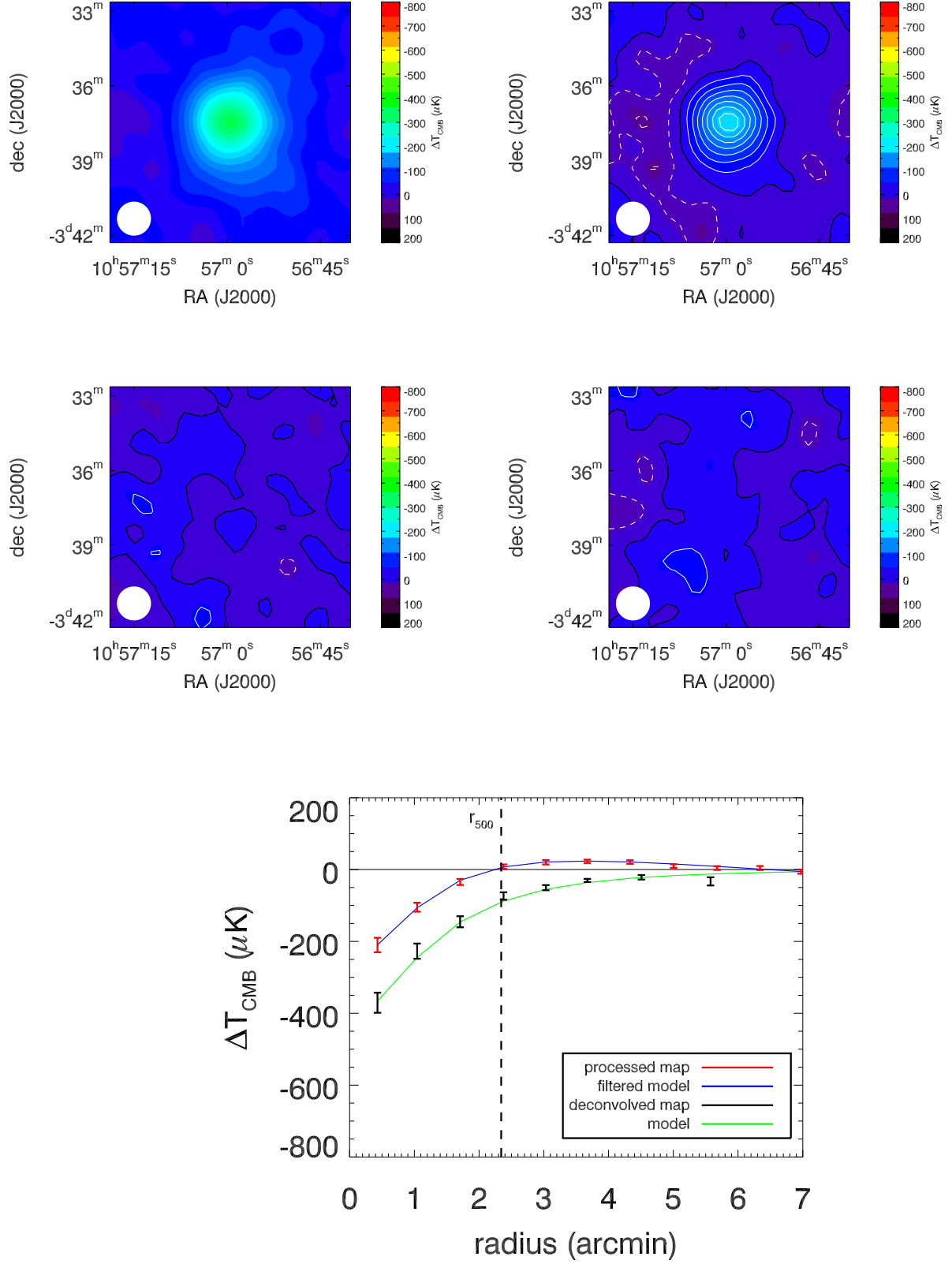


FIG. A5.— MS 1054.4-0321; from left to right and top to bottom we show the deconvolved image of the cluster, the processed image of the cluster, the residual map between the processed image of the cluster and the best-fit elliptical Nagai model, one of the 1000 noise realizations for the processed data, and a binned radial profile. The contour lines represent a S/N of 2, 4, ...

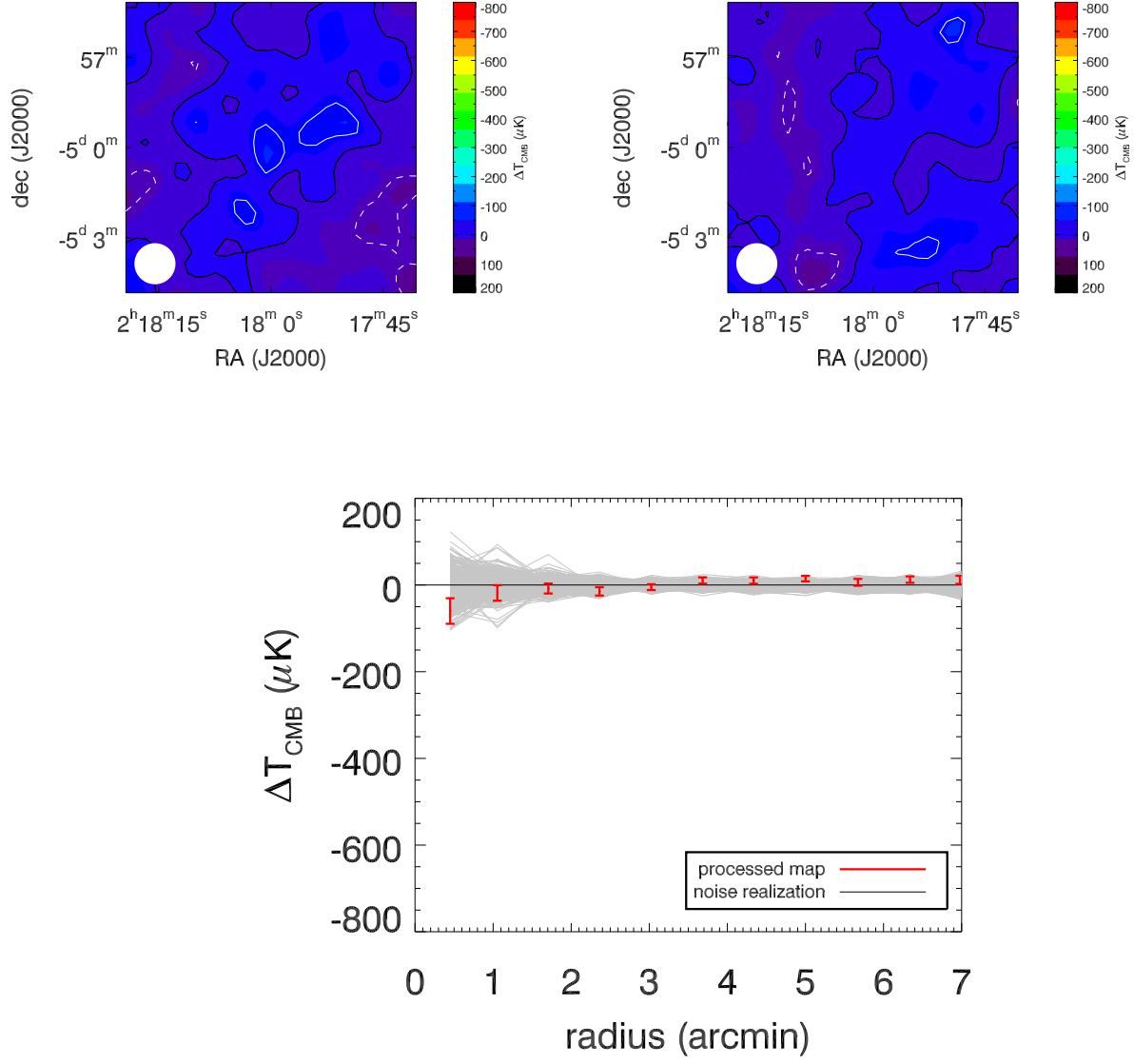


FIG. A6.— SDS1; from left to right and top to bottom we show the processed image of the field, one of the 1000 noise realizations for the processed data, and a binned radial profile. The contour lines represent a S/N of 2, 4, ... The thin grey lines show the radial profiles for each of the 1000 noise realizations.